iScience

CellPress
REVIEWS

Review

Chalcogenide Taper and Its Nonlinear Effects and Sensing Applications

Song Gao[1] and Xiaoyi Bao[1,*]

The nonlinear coefficient of chalcogenide glass is 200–1000 times larger than that of silica glass, and it is transparent in the 1–15 μm wavelength windows, which makes the nonlinear effects happen at much low power with a short length in near- and mid-infrared wavelength window. With tapered chalcogenide fibers, the power density in the core and the waveguide nonlinearity can be enhanced to make nonlinear signal processing unit at a compact size. The threshold of Raman scattering and supercontinuum generation is reduced due to the enhanced Kerr effect and enhanced optical power intensity. Phase-matching condition required in four-wave mixing (FWM) can be realized by tailoring fiber structures to engineer the chromatic dispersion, which enables new wavelengths creation over a large range at mW power and sub-meter length. The guided acoustic waves and longitudinal acoustic waves can be generated and detected in mW power with chalcogenide tapers. The high power density in the microwires and the high photosensitivity of chalcogenide glass in the 1550 nm band enable the inscription of FBGs in the fiber directly. The chalcogenide microwires are fragile and the core diameter cannot be tapered down to sub-microns, which can be mitigated by polymer coating that can provide mechanical strength. Polymers not only provide high mechanical strength as the coating and cladding materials but also bring over 10 times larger thermal expansion than chalcogenide cores, which enhances the sensor prospect of the chalcogenide fibers for temperature, strain, and acoustic sensing. This work reviews the present and emerging trends in investigation of chalcogenide tapers, mainly focusing on the fabrication procedure of chalcogenide microwires, the nonlinear effects, and sensing applications.

INTRODUCTION

Silica fibers have high attenuation up to 60 dB/m at wavelengths longer than 3 μm (Humbach et al., 1996; Kitamura et al., 2007; Yu et al., 2012), which makes it not applicable in the applications in the mid-infrared (mid-IR) wavelength range (2–25 μm). Chalcogenide glass containing one or more chalcogens (sulfur(S), selenium (Se), and tellurium(Te), but excluding oxygen) is a good candidate because it has wide transparency with the transmission window from 0.5 to 25 μm (Sanghera et al., 2001, 2002; Schliesser et al., 2012), which implies potential applications based on the mid-IR sources. As shown in Figure 1, the long wavelength cut-off edges of chalcogenide bulk materials are extended between 12 and 20 μm depending on the mass of anionic elements (Tao et al., 2015). Besides the low loss in the mid-IR range, chalcogenide glass has the material nonlinearity (n_2) 200–1000 times larger than that of the silica glass at wavelength of 1,550 nm (Letokhov, 1968; Li et al., 2016b; Slusher et al., 2004).

Table 1 lists some parameters of silica and chalcogenide fibers. Nonlinear applications in near- and mid-IR region based on chalcogenide fibers have been widely investigated, such as ultrafast all-optical switches (Asobe et al., 1993), Raman lasers (Ahmad and Rochette, 2014; Bernier et al., 2013), supercontinuum generation (Dai et al., 2018), strong stimulated Brillouin scattering (Abedin, 2005), mode-locked lasers (Al-Kadry et al., 2015a), chalcogenide fiber-based mid-IR sources (Sanghera et al., 2009), and slow and fast light in high nonlinear chalcogenide fibers (Song et al., 2006). As_2Se_3, as one material that has the highest material nonlinearity n_2 among all chalcogenide glass at 1,550 nm, attracts extensive attention.

The waveguide nonlinearity γ is defined as $\gamma = k_0 n_2/A_{eff}$, where n_2 is the material nonlinearity, $k_0 = 2\pi/\lambda$ is the wave-number with λ being the wavelength, and A_{eff} is effective mode area. To achieve high-efficiency nonlinear effects in a waveguide, one approach is to use the material with high nonlinearity such as chalcogenide glasses as the core material with a high value of n_2 (Asobe, 1997; Asobe et al., 1993; Eggleton et al., 2011; Sanghera et al., 2009, 2010; Slusher et al., 2004). Another approach is to reduce the value of A_{eff} by decreasing the diameter of a fiber, which can also engineer the waveguide dispersion of the waveguide (Birks et al., 2000; Brambilla, 2010; Brambilla et al., 2009; Gattass et al., 2006). Fabricating microwires

[1]University of Ottawa, Department of Physics, Ottawa, ON, K1N 6N5, Canada

*Correspondence: xbao@uottawa.ca

https://doi.org/10.1016/j.isci.2019.100802

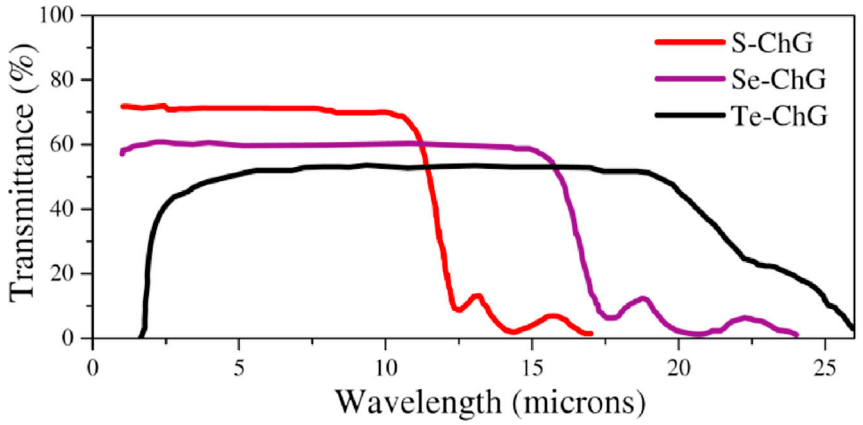

Figure 1. Typical Infrared (IR) Transmission Spectra of S-, Se-, and Te-based Chalcogenide (ChG) Bulk Samples
Image from Tao et al. (2015).

with a large contrast of refractive index between the core and the cladding can further reduce the effective mode area A_{eff} due to more light confined in the core area to enhance the waveguide nonlinearity, which brings out the chalcogenide-polymer tapers (Baker, 2013; Baker and Rochette, 2010; Rochette and Baker, 2014). Coating chalcogenide fibers with polymers requires that the polymer should have low loss at the optical wavelength to be transmitted, low refractive index to confine more light in the core, and similar transition temperature to the chalcogenide fibers (Li et al., 2016a). Many polymers such as poly (methyl methacrylate) (PMMA) polycarbonate (PC), cyclo olefin polymer (COP), and fluorine-based CYTOP are good candidates as a cladding material. For example, the refractive index of PMMA is 1.478 at 1,550 nm (Jensen et al., 2005; Kuzyk, 2018; Silva-López et al., 2005; Yuan et al., 2011) that is much smaller than that of chalcogenide glasses, which confines light tightly in the core area and enhances the waveguide nonlinearity in the chalcogenide-PMMA microwires. A waveguide nonlinearity with γ =176 $W^{-1}m^{-1}$ is achieved in chalcogenide-PMMA microwires by tapering the core diameter down to 0.45 μm (Kenny et al., 1991). The transparent wavelength window of PMMA polymer is from visible region to 2.2 μm (Li et al., 2016b), but the PMMA-cladded chalcogenide microwires have high loss between 0.30 dB/cm and 0.83 dB/cm from 1.30 μm to 2.20 μm and an absorption peak at ~1.65 μm due to the vibrational transition of C-H bond (Li et al., 2016a). To avoid the vibrational transition of C-H bond in the hydrogen-based polymers, the microwire with CYTOP cladding is fabricated with the low attenuation up to a wavelength of 4.3 μm (Li et al., 2016a). The polymer fibers can be used for nonlinear and sensing applications (Emiliyanov et al., 2006; Jensen et al., 2005; Yuan et al., 2011), which is not the subject of the current review. The microwires made with chalcogenide fibers are the key subject of this review work, especially focusing on the demonstrated high nonlinearity-associated effects and sensing capability enhanced by polymer coatings in chalcogenide-polymer tapers.

Device and Material	Refractive Index	n_2 (m^2/W)	Transmission Range (μm)	Loss (dB m^{-1})
Silica fiber	1.46 @1.55 μm (Agrawal, 2000)	2.36×10^{-20} @1.55 μm (Kim et al., 1994)	0.24–2 (Li, 2012)	0.0002 @1.55 μm (Miya et al., 1979)
As_2S_3 fiber	2.4 @1.55μm (Florea et al., 2009; Rodney et al., 1958)	3×10^{-18} @2 μm (Lamont et al., 2008)	0.7–6 (Harrington, 2004; Kanamori et al., 1984)	0.2 @1.55 μm (Miyashita and Terunuma, 1982)
As_2Se_3 fiber	2.83 @1.55 μm (Boudebs et al., 2004)	1.1×10^{-17} @2 μm (Fu et al., 2005)	1–10 (Dai et al., 2018; Wang et al., 2018)	0.85 @1.55 μm (Baker and Rochette, 2012; Slusher et al., 2004)
Te-based fiber (Tao et al., 2015)	3.2 @2 μm	~10^{-17}	2–12	3 @10 μm
GeAsSe PCF	2.6 @2 μm (Dantanarayana et al., 2014)	5.3×10^{-17} @2 μm (Xing et al., 2016)	–	0.5 @2 μm (Xing et al., 2016)

Table 1. Typical Optical Parameters of Silica Fiber and Several Chalcogenide Fibers

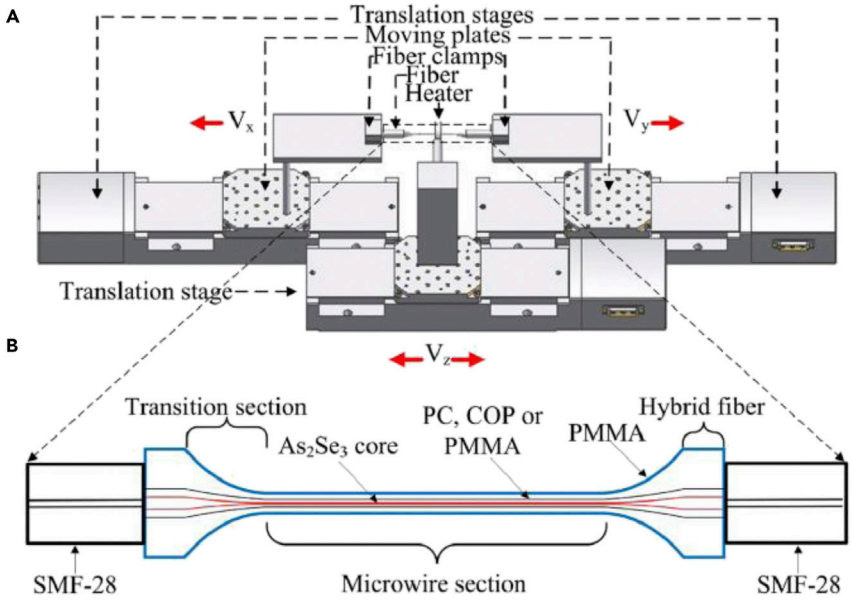

Figure 2. Taper Fabrication Setup

Schematic of (A) polymer-cladded As_2Se_3 micro-taper fabrication setup and (B) polymer-cladded As_2Se_3 micro-taper coupled to single-mode fibers; image from Li et al. (2016b).

FABRICATION PROCEDURE

Birks (Birks and Li, 1992) reported a tapering approach for shaping a fiber taper by changing the hot-zone length as the fiber is stretched at both ends. Baker successfully fabricated the first hybrid chalcogenide-PMMA taper consisting of an As_2Se_3 core and a PMMA cladding (Baker and Rochette, 2010) and also reported a generalized heat-brush tapering approach in which the ratio of the feed and draw velocities changes at every tapering sweep (Baker and Rochette, 2011).Li (Li et al., 2016b) fabricated the PC- and COP-coated As_2Se_3 microwires. The fabrication procedure of hybrid-chalcogenide-polymer tapers includes five steps: (1) preparation of the chalcogenide rods and polymer tubes, (2) preform fabrication, (3) fiber drawing, (4) polishing and coupling, and (5) microwire fabrication. The details are described thoroughly in Baker (2013) and Gao (2019). Figure 2A shows a schematic of polymer-cladded As_2Se_3 microwire fabrication setup. Figure 2B shows the various sections of a micro-taper with both ends permanently butt-coupled to single-mode fibers (SMF-28) using UV-cured epoxy.

Figure 3 shows an image of different sections of an As_2Se_3-PMMA taper whose ends are permanently butt-coupled to single-mode fibers using UV-cured epoxy. Various sections of the As_2Se_3-PMMA taper are labeled including the connection between SMFs and hybrid fibers, hybrid fibers, transition sections, and 5-cm-long microwire section.

Chalcogenide fibers have high material nonlinearity due to the chalcogenide glass as the core material with a high nonlinear coefficient. For instance, As_2Se_3 glass has a high nonlinear coefficient that is ~930 times larger than that of silica glass. The nonlinearity of the tapered chalcogenide fibers is further enhanced with engineered chromatic dispersion. The effective material nonlinearity is given by (Afshar and Monro, 2009)

$$\overline{n}_2 = \frac{\varepsilon_0}{\mu_0} \frac{\iint_{\infty} n_0^2(x,y) n_2(x,y) \left(2|\vec{E}|^4 + |\vec{E}^2|^2\right) dA}{3\iint_{\infty} |[\vec{E} \times \vec{H}^*] \cdot \hat{z}|^2 dA}$$

where ε_0 and μ_0 are the electric permittivity and the magnetic permeability of free space, respectively, n_0 is the refractive index, n_2 is the material nonlinearity, E and H are the electric and magnetic fields, respectively, z is the direction of propagation, and A is the transverse surface area. The chromatic dispersion is given by (Agrawal, 2000)

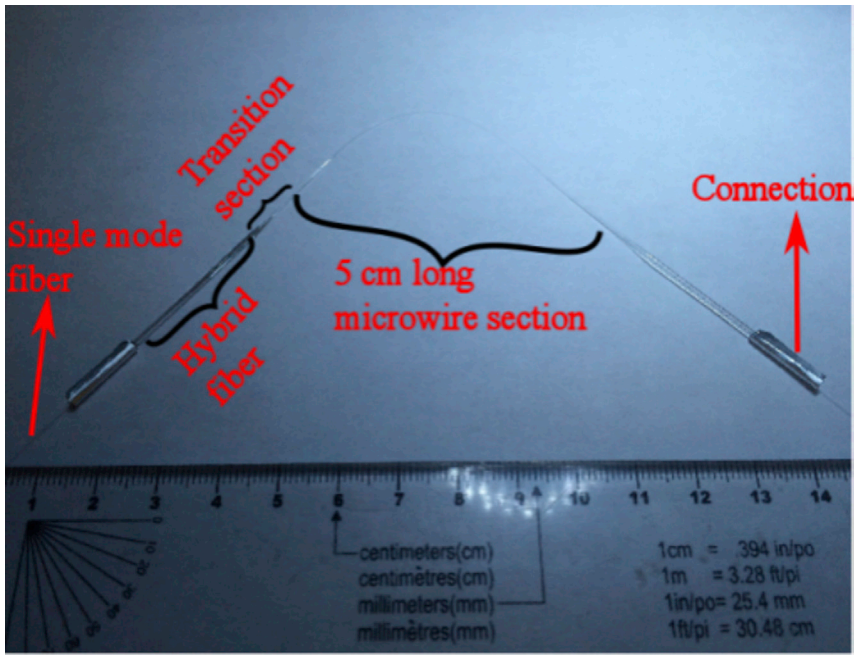

Figure 3. An Image of an As_2Se_3-PMMA Micro-Taper
Image from Gao (2019).

$$D_c = -\frac{\lambda}{c}\frac{d^2 n_{eff}}{d\lambda^2}$$

where λ is the wavelength, c is the velocity of light in free space, and n_{eff} is the effective refractive index.

Figure 4 shows the calculated waveguide nonlinearity parameter γ and chromatic dispersion D_c of hybrid As_2Se_3-PMMA tapers as a function of core diameter at wavelength of 1,550 nm (Baker and Rochette, 2010). The large difference of refractive index between polymer cladding and chalcogenide core confines most of the light in the core and reduces the power consumption for nonlinear effects. Furthermore, polymer cladding can engineer the waveguide dispersion to change the total dispersion in the microwires. Al-Kadry (Al-Kadry et al., 2015b) fabricated PMMA-coated As_2S_3 microwires. At core diameter of 0.58 μm, the group velocity dispersion of the microwires shifts to normal at 1,550 nm rather than in the anomalous regime of the air-coated As_2S_3 microwires. Table 2 lists some parameters such as waveguide nonlinearity γ and zero-dispersion wavelength of some chalcogenide tapers.

NONLINEAR EFFECTS IN CHALCOGENIDE TAPERS

In this section, the following nonlinear effects in chalcogenide tapers are reviewed.

- Four-wave mixing
- Modulation instability
- Fiber Bragg gratings and antisymmetric long-period grating
- Forward Brillouin scattering
- Stimulated Brillouin scattering
- Raman scattering
- Nonlinear polarization-rotation-based mode-locked laser
- Supercontinuum generation

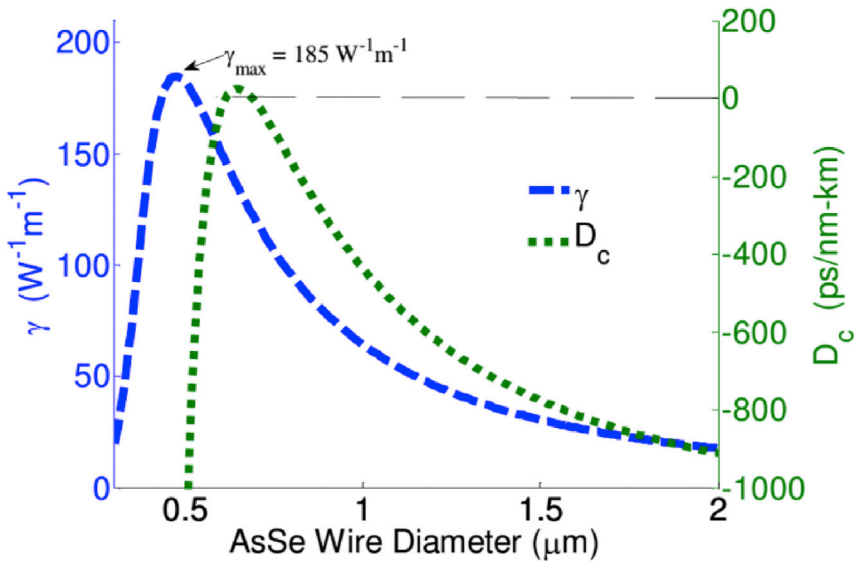

Figure 4. The Calculated Waveguide Nonlinearity and Chromatic Dispersion of the Hybrid As_2Se_3-PMMA Taper as a Function of Core Diameter at a Wavelength of 1,550 nm
Image from Baker and Rochette (2010).

Four-Wave Mixing

High-efficiency four-wave mixing requires large nonlinearity in the anomalous dispersion regime to satisfy the phase-matching condition. Chalcogenide microwires satisfy these conditions with high material nonlinearity of chalcogenide glass and high waveguide nonlinearity, as well as anomalous dispersion regime achieved by the fiber diameter reduction. Because chalcogenide fibers usually have a large normal material dispersion at the pump wavelength, many research focuses on the manipulation of waveguide structures such as tapering structure and photonic crystal fiber (PCF) structures to change the waveguide dispersion to compensate for the normal material dispersion.

Ahmad (Ahmad and Rochette, 2012b) investigated four-wave mixing based on a 10-cm-long single-core As_2Se_3-PMMA taper with As_2Se_3 core diameter of 1.01 μm. The wavelength conversion bandwidth is 190 nm, which is a 30 times improvement over the previous demonstration, thanks to the engineered dispersion and an enhanced nonlinear coefficient by tapering down the fiber to a microwire. Ahmad (Ahmad and Rochette, 2012a) also demonstrated an optical oscillator based on four-wave mixing in a 10-cm-long single-core As_2Se_3-PMMA taper with As_2Se_3 diameter of 1.01 μm. The gain medium of As_2Se_3-PMMA microwire was inserted in a fiber loop and two oscillating wavelengths at a Stoke and anti-Stoke wavelength shift of +53 nm and −50 nm were observed. The optical oscillator oscillated at a low peak pump with a power threshold of 21.6 dBm and with a total conversion efficiency of >19%. Abdukerim (Abdukerim et al., 2016) reported an optical oscillator based on four-wave mixing with a tunable wavelength range of 290 nm. These results are achieved by the combination of both Stokes and anti-stokes in a 10-cm-long As_2Se_3-COP microwire with As_2Se_3 core diameter of 1.47 μm. Combination of high optical confinement due to the large difference of refractive index between the As_2Se_3 core and COP cladding and high nonlinearity of As_2Se_3 leads to a high waveguide nonlinearity of $\gamma = 24\ W^{-1}m^{-1}$ in the microwire, and the zero-dispersion wavelength is shifted to 1.875 μm. Overall, the high efficiency and ultra-broadband four-wave mixing in chalcogenide-polymer microwires can lead to interesting applications in lasers, optical sensing systems, and optical communication devices from near- to mid-infrared regions.

A chalcogenide PCF taper was proposed to increase the waveguide nonlinearity for wavelength conversion based on four-wave mixing (Le et al., 2012). Xing (Xing et al., 2017) used a 1-m-long tapered GeAsSe PCF fiber with a core diameter of 1.5 μm to achieve continuous-wave-pumped four-wave mixing by combining high nonlinearity, low dispersion, low loss, and single-mode behavior, which benefits from the engineered GeAsSe PCF structure. Figure 5 shows the schematic of the dispersion-engineered tapered GeAsSe PCF fiber.

Material	Taper Length	Taper Diameter	Zero-Dispersion Wavelength	Waveguide Nonlinearity γ	Nonlinear Effects or Application	Year
As_2Se_3 taper	18 mm	1.2 μm	~1,550 nm	68 $W^{-1}m^{-1}$ @1,550 nm	Self-phase Modulation	2007 (Mägi et al., 2007)
As_2Se_3-PMMA taper	7 cm	0.8 μm	1,550 nm	133 $W^{-1}m^{-1}$ @1,552.4 nm	Self-phase Modulation	2010 (Baker and Rochette, 2010)
As_2S_3 taper	50 mm	1.3 μm	~1.4 μm	12.4 $W^{-1}m^{-1}$ @1,550 nm	Supercontinuum Generation	2011 (Hudson et al., 2011)
As_2Se_3-PMMA taper	10 cm	1.01 μm	1,536 nm	76 $W^{-1}m^{-1}$ @1,536 nm	Four-wave Mixing	2012 (Ahmad and Rochette, 2012b)
As_2Se_3-PMMA taper	14 cm	3.6 μm	2,830 nm	7 $W^{-1}m^{-1}$ @2,620 nm	Modulation Instability	2014 (Godin et al., 2014)
As_2Se_3-PMMA taper	13 cm	1 μm	1,529 nm	99 $W^{-1}m^{-1}$ @1,532 nm	Raman laser	2014 (Ahmad and Rochette, 2014)
As_2S_3-PMMA taper	10 cm	1.7 μm	1,625 nm	11.3 $W^{-1}m^{-1}$ @1,550 nm	Mode-locked laser	2015 (Al-Kadry et al., 2015a)
As_2S_3-PMMA taper	3 mm	0.58 μm	1,300 nm	54 $W^{-1}m^{-1}$ @1,550 nm	Supercontinuum Generation	2015 (Al-Kadry et al., 2015b)
GeAsSe PCF taper	27 cm	4 μm	2 μm	1.688 $W^{-1}m^{-1}$ @1,981 nm	FWM-based wavelength converter	2016 (Xing et al., 2016)
As_2Se_3-COP taper	10 cm	1.47 μm	1875 nm	24 $W^{-1}m^{-1}$ @1,940 nm	Parametric oscillator	2016 (Abdukerim et al., 2016)
GeAsSe PCF taper	1 m	1.5 μm	2.1 μm	10 $W^{-1}m^{-1}$ @2 μm	Parametric amplification	2017 (Xing et al., 2017)

Table 2. Typical Optical Parameters of Chalcogenide Tapers

In situ fabrication of far-detuned fiber wavelength converter has been demonstrated by *in situ* tracking of the four-wave mixing in an As_2Se_3 microwire (Alamgir et al., 2019). The pump wavelength is set to 1.938 μm and probe wavelength is tuned from 2.34–2.49 μm. As the diameter of the As_2Se_3 is tapered down, the waveguide dispersion balances the material dispersion to satisfy the phase-matching conditions and maximize the gain spectrum. Figure 6 shows the measured idler spectra at the different stretching length of the tapering process. As the diameter decreases, the group velocity dispersion changes from normal to anomalous, and the minima and maxima gain spectra shift toward shorter wavelength.

Modulation Instability

Modulation instability (MI) is a process where weak modulations on a high-power optical signal are amplified with a buildup of new optical frequencies on both sides of the pump signal by phase matching the pump signal with light at newly generated wavelengths. It has been reported that MI is achieved in

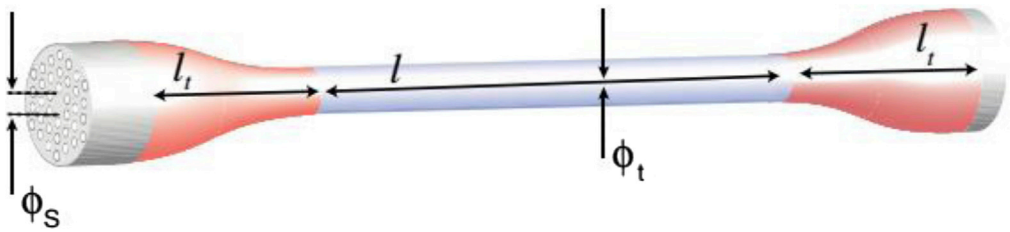

Figure 5. Schematic of the Dispersion-Engineered Tapered GeAsSe PCF Fiber
Image from Xing et al. (2017).

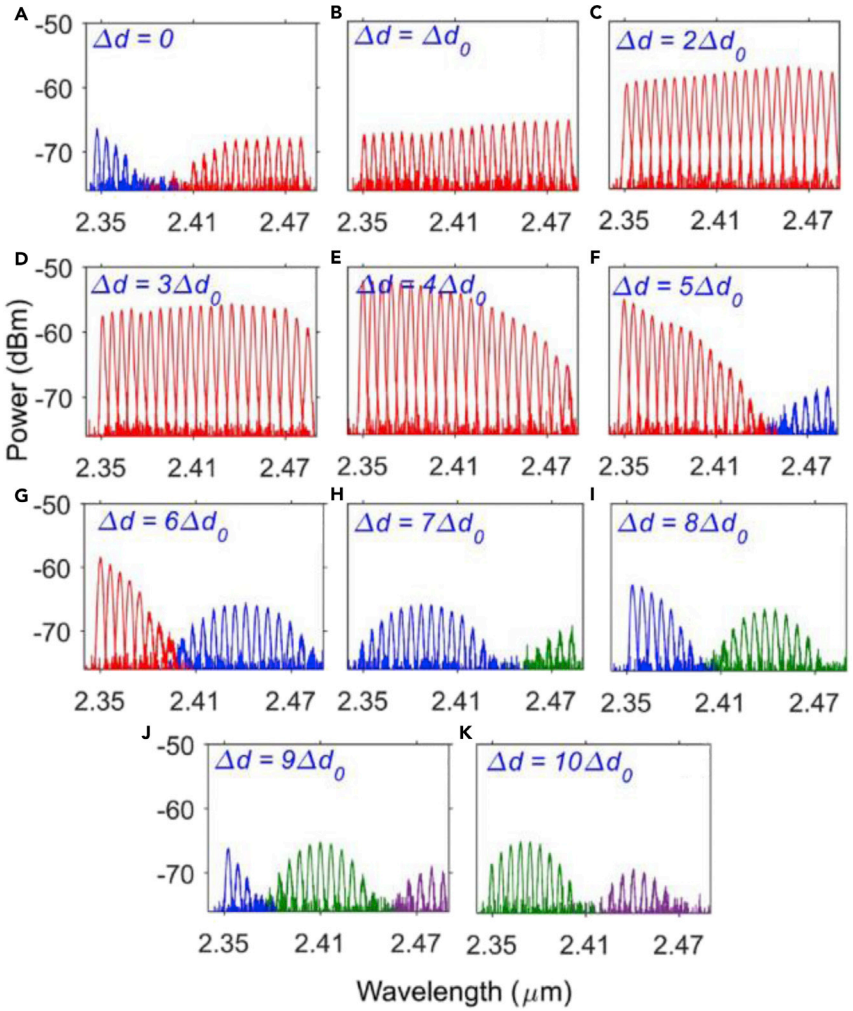

Figure 6. Measured Idler Spectra at the Different Stretching Length of the Tapering Process

(A–K) Measured idler spectra at different times of the tapering process as the microwire GVD changes from normal to anomalous. Δd is defined as $\Delta d = k\,\Delta d_0$, where k is an integer and Δd_0=8 nm. Image from Alamgir et al. (2019).

single-core fibers in the anomalous dispersion regime where phase matching can be achieved (Ahmad and Rochette, 2012b; Tai et al., 1986). In the normal dispersion regime, MI can also be achieved in silica-based PCF fibers (Harvey et al., 2003; Pitois and Millot, 2003) and single-mode fibers (Harvey et al., 2003; Pitois and Millot, 2003). In chalcogenide tapers, two methods to achieve MI in normal dispersion regime have been proposed: one is to utilize a high-order group velocity dispersion profile such as the fourth-order dispersion β_4 to meet the phase-matching conditions (Godin et al., 2014; Li et al., 2017); the other is to modify the waveguide structure such as dual-core structure to induce coupling of different modes for phase-matching conditions to balance the normal dispersion (Gao, 2019).

Godin (Godin et al., 2014) demonstrated that MI occurs in normal dispersion regime through the negative fourth-order dispersion from pumping at a wavelength of 2.6 μm based on a 14-cm-long As_2Se_3–PMMA taper. The frequency detuning is up to ~30 THz. Li (Li et al., 2017) further extended the frequency detuning to 49.3 THz based on a 10-cm-long As_2Se_3–CYTOP taper with a core diameter of 1.68 μm, which is shown in Figure 7.

Manipulating the waveguide structure, such as dual-core structure, is another approach for MI in the normal dispersion regime. Theoretical analysis of MI in dual-core fibers has been reported (Agrawal, 1987; Li et al.,

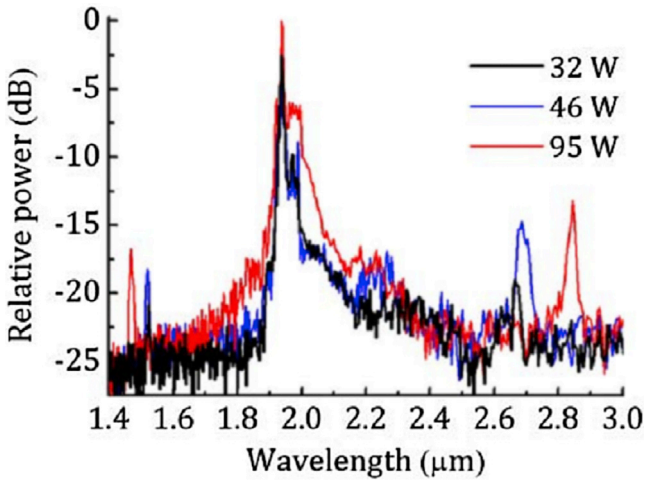

Figure 7. Measured Spectra of MI in a 10-cm-Long As_2Se_3 Taper with a Core Diameter of 1.625 μm
Image from Li et al. (2017).

2011; Rothenberg, 1990). Based on the coupled-mode theory, the evolution of the electric field along the dual-core fiber is described by the coupled nonlinear Schrödinger equations (Li et al., 2011):

$$i\frac{\partial a_1}{\partial z}-\frac{1}{2}\beta_2\frac{\partial^2 a_1}{\partial t^2}+\gamma|a_1|^2a_1+Ca_2+iC_1\frac{\partial a_2}{\partial t}=0$$

$$i\frac{\partial a_2}{\partial z}-\frac{1}{2}\beta_2\frac{\partial^2 a_2}{\partial t^2}+\gamma|a_2|^2a_2+Ca_1+iC_1\frac{\partial a_1}{\partial t}=0$$

where a_i is the slowly varying electric-field envelope in core i; i = 1 or 2; z and t are the propagation distance and the time coordinate, respectively; β_2 measures the group velocity dispersion (GVD) at the carrier frequency; γ is the waveguide nonlinearity parameter; C is the coupling coefficient; and $C_1=dC/d\Omega$ is the coupling coefficient dispersion, which shows that the coupling coefficient between the two cores depends on the optical wavelength (Chiang, 1997a, 1997b). The coupling coefficient C and coupling coefficient dispersion C_1 are induced to make MI obtain gain in normal dispersion regime due to the dual-core structure.

Gao (Gao, 2019) reported the experimental observation of MI in the normal dispersion regime in a tapered dual-core As_2Se_3-PMMA fiber. The sample is a 10-cm-long dual-core microwire with As_2Se_3 core diameter of 1.5 μm and a PMMA cladding diameter of 84.7 μm. Figure 8A presents the setup utilized for the observation of modulation instability in the tapered dual-core As_2Se_3-PMMA fiber using pulses with high peak power. Figure 8B presents the measured spectra as the increase of input pulse power. As the laser power increases, the spectrum of the pulse broadens by self-phase modulation due to the high nonlinear coefficient in the dual-core fiber. And two peaks, peak A and peak B, arise in the modulation instability gain spectra due to the strong wavelength dependence of the coupling coefficient in the dual-core fiber (Li et al., 2011). The dual-core structure induces the coupling of modes in two cores to fulfill phase-matching conditions. Modulation instability in dual-core fibers can be used for enhanced parametric amplification, broadly tunable lasers, and efficient entangled photon generations.

Fiber Bragg Gratings and Antisymmetric Long-Period Grating

Fiber Bragg gratings (FBGs) can be regarded as a linear medium, which is used for sensing in various application fields such as temperature measurement (Kersey et al., 1993), strain detection (Torres et al., 2011), and biomedical applications (Kanellos et al., 2010). They also can be viewed as nonlinear devices that can be used for pulse switching (Lee and Agrawal, 2003), pulse-shaping (Petropoulos et al., 2001), and slow light (Boyd, 2011).

Ahmad (Ahmad et al., 2011) reported the inscription of side-written Bragg grating employing a He–Ne laser light at a wavelength of 633 nm to write Bragg grating reflectors at the wavelength of 1,550 nm band due to the two-photon absorption effect in a 3-cm-long single-core As_2Se_3-PMMA tapers with a core diameter of 1 μm. The setup is sketched in Figure 9. In this case, the inscription of the FBG is induced due to the

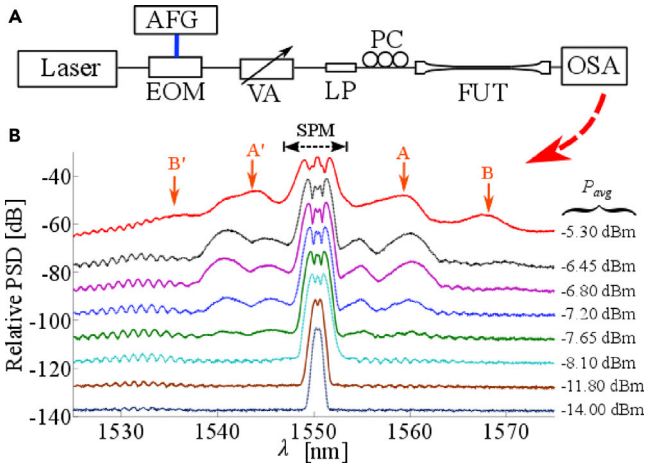

Figure 8. Experimental Study on Modulation Instability

(A) Schematic of the modulation instability characterization setup and (B) relative values of the measured spectra at the output of the dual-core fiber as the input pulse power increases. Image from Gao (2019).

absorption of light with wavelength equal or close to a material band gap. Using a laser source at a wavelength of 1,550 nm to inscribe a Bragg grating in a 4-cm-long single-core As_2Se_3-PMMA taper with a core diameter of 1 μm has also been reported, and the photosensitivity thresholds related to exposure intensity and exposure time are quantified (Ahmad and Rochette, 2011). The two counter-propagating waves form standing waves in the microwire section and induce refractive index change periodically along the fiber to write a Fiber Bragg grating. The energy transfers from 1,550 nm photons to the chalcogenide glass due to the two-photon absorption effect. This high absorption at 1,550 nm allows for a quick grating fabrication process.

Baker (Baker et al., 2017) demonstrated that transmission of optical pulses centered at a wavelength of 1,550 nm through a tapered dual-core As_2Se_3-PMMA fiber inscribes an antisymmetric long-period grating due to photosensitivity of As_2Se_3. Figure 10 illustrates the refractive index distribution of an antisymmetric long-period grating.

Figure 11 shows the schematic of the setup for inscription and characterization of an antisymmetric long-period grating in a tapered dual-core As_2Se_3-PMMA fiber and the evolution of the transmission spectrum as the increase of the cumulative exposure time. The phase difference $\Delta\phi(\lambda)$ between the even and

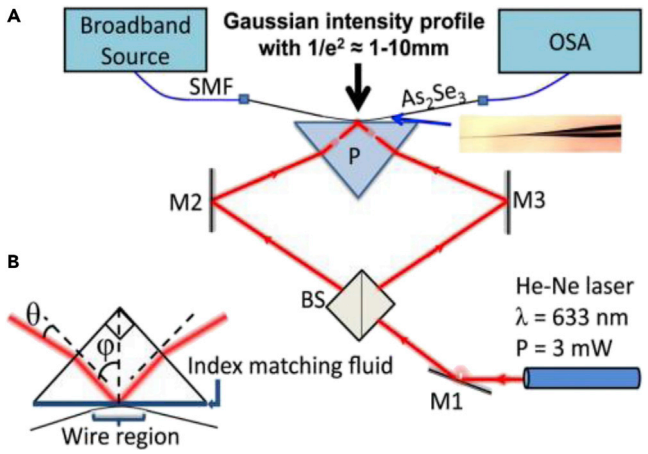

Figure 9. Experimental Setup for the Side-Written Bragg Inscription

(A) Experimental setup for the Bragg grating photo-inscription and in situ monitoring of the process. (B) Detailed schematic of the prism. Image from Ahmad et al. (2011).

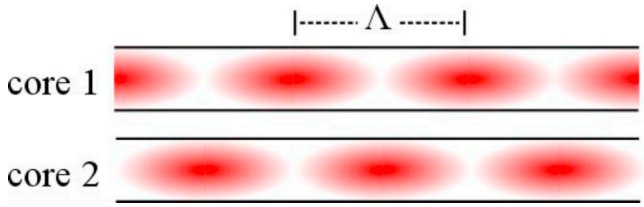

Figure 10. Refractive Index Distribution of an Antisymmetric Long-Period Grating in a Dual-Core As_2Se_3-PMMA Taper

Image from Baker et al. (2017).

odd modes in the antisymmetric long-period grating has slow variation near the resonance wavelength of λ_r = 1,550 nm, indicating effective group-velocity matching. Group-velocity matching can be used for enhanced nonlinear processing of sub-picosecond pulses due to a short pulse walk-off and for increased efficiency of phase-matched four-wave mixing. Furthermore, fast variation of $\Delta\phi$ at λ_r implies that the phases of even and odd modes have fast variations with wavelength, indicating the potential for inducing slow light, which will further enhance the waveguide nonlinearity parameter.

Forward Brillouin Scattering

Tight confinement of longitudinal and transverse acoustic waves can lead to strong interactions with light waves in a fiber core. Acousto-optic interactions (Biryukov et al., 2002; Kang et al., 2009; Peral and Yariv, 1999; Russell et al., 1990, 1991; Shelby et al., 1985; Wang et al., 2011) have been studied extensively such as forward-stimulated Brillouin scattering and backward-stimulated Brillouin scattering in silica fibers. Due to the interaction between the incident light and acoustic waves propagating in the cross-sectional area of the fiber, lights are scattered propagating with the pump light in the same direction, which is known to be forward-stimulated Brillouin scattering (FSBS) that accompanies multiple spectral peaks caused by acoustic resonance. Two types of acoustic modes occur in FSBS: one is the radial mode that perturbs the refractive index of the fiber cross-section, and the other is the torsional-radial mode that perturbs not only the refractive index but also the birefringence (Auld, 1973; Engan et al., 1988; Hayashi et al., 2017; Shelby et al., 1985; Thurston, 1992).

Gao (Gao, 2019) investigated the radial acoustic modes in both silica single-mode fibers and single-core As_2Se_3-PMMA tapers that were placed in a Sagnac loop. Figure 12A shows the signal amplitude as a function of time when the single-mode fiber without coating was exposed in the air. A stimulated acoustic

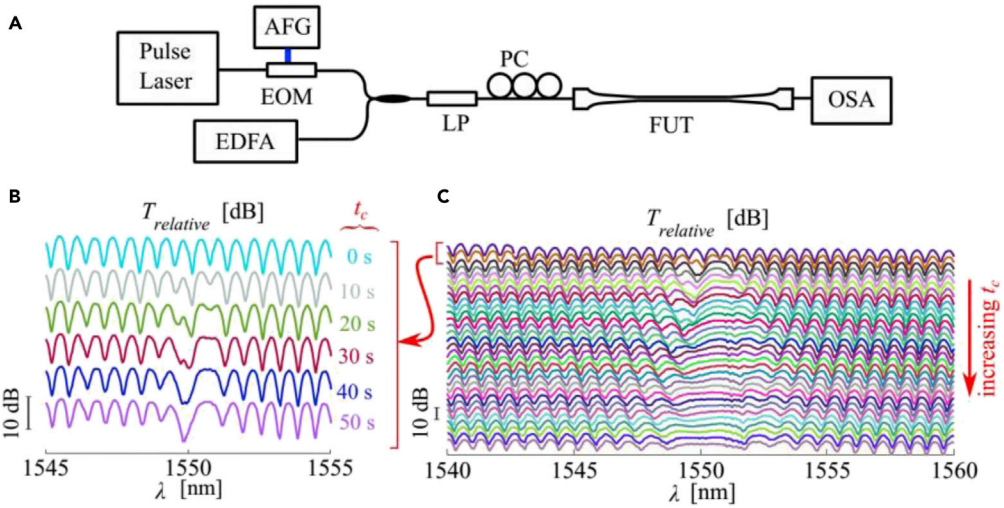

Figure 11. Experimental Study on the Inscription of Antisymmetric Long-Period Gratings

(A) Schematic setup for inscription of an antisymmetric long-period grating.

(B) Initial growth of the transmission spectrum as the increase of exposure time.

(C) Evolution of transmission spectrum as the increase of exposure time. Image from Baker et al., (2017).

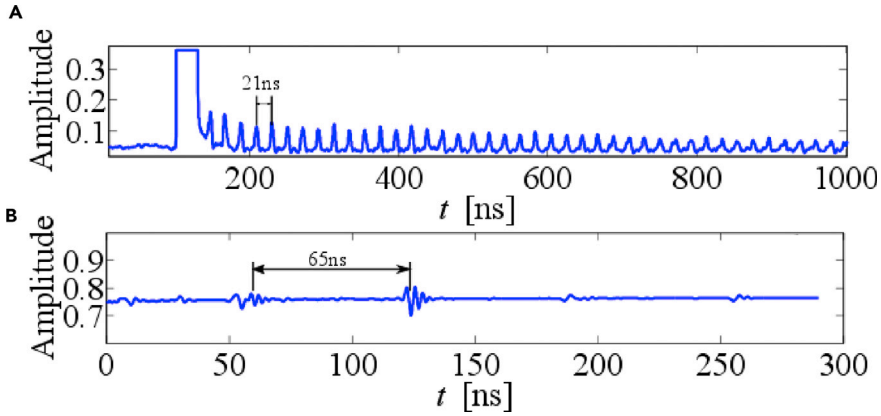

Figure 12. Experimental Results of Radial Acoustic Modes

Measured power of the signal as a function of time t in the oscilloscope when the fiber under test was (A) 15-m-long single-mode fiber without coating and (B) 10-cm-long As_2Se_3-PMMA taper, respectively. Image from Gao (2019).

impulse radiates outward from the core to the out boundary of the cladding. Part of the acoustic wave is reflected by the boundary between the cladding and the air and propagates back toward the core. The travel time from the core to the boundary of cladding is ~21 ns that is determined by the cladding diameter and the acoustic velocity in the cladding. Similarly, a 10-cm-long single-core As_2Se_3-PMMA taper with As_2Se_3 core diameter of 3 μm and PMMA diameter of 169.5 μm was placed in the Sagnac loop as fiber under test. Figure 12B shows the measured power of the signal as a function of time showing that the echo period is about ~65 ns that is determined by the acoustic velocity in PMMA of 3,800 m/s (Hayashi et al., 2011) and the diameter of PMMA.

Torsional-radial acoustic modes are also investigated in a 1.5-km-long single-mode fiber and a 60-cm-long As_2Se_3-PMMA taper with As_2Se_3 diameter of 1.06 μm and PMMA cladding diameter of 60 μm, respectively (Gao, 2019). A peak at 108.2 MHz was observed shown in Figure 13A that corresponds to the $TR_{2,5}$ mode in silica single-mode fibers. Figure 13B shows the torsional-radial acoustic modes of the As_2Se_3-PMMA taper with a peak frequency of ~292 MHz.

Based on the measurements of radial- and torsional-radial-guided acoustic modes, many sensing applications have been investigated such as impedance measurement (Antman et al., 2016) and absolute diameter characterization (Jarschel et al., 2018). A new approach for humidity sensing based on As_2Se_3-PMMA tapers can be achieved due to the impedance changed in the PMMA cladding induced by the water absorption property of the PMMA material.

Stimulated Brillouin Scattering

Stimulated Brillouin scattering (SBS) is caused by the nonlinear interaction among the pump, Stokes fields, and a longitudinal acoustic wave by the electrostriction process (Agrawal, 2000).

Stimulated Brillouin scattering in single-mode As_2Se_3 chalcogenide fibers has been observed with the Brillouin frequency shift of 7.95 GHz and the gain bandwidth of 13.2 MHz at 1,560 nm (Abedin, 2005). Beugnot (Beugnot et al., 2014) investigated the influence of the diameter of chalcogenide tapers and PMMA coating on the SBS spectrum, which shows that the Brillouin frequency shift and threshold of the stimulated Brillouin scattering significantly increase with the wire diameter due to acoustic damping in the PMMA cladding.

However, in tiny waveguides, the waveguide boundaries induce a strong coupling of shear phonons, longitudinal phonons, and guided acoustic phonons, resulting in much richer dynamics of light interaction with hybrid acoustic modes. Saxena (Saxena et al., 2019b) investigated the SBS using a BOTDA system in As_2Se_3-PMMA tapers. Simultaneous generation of stimulated Brillouin scatting and guided acoustic wave Brillouin scattering from electrostriction was observed in a 60-cm-long As_2Se_3-PMMA taper with As_2Se_3 core diameter of 2 μm. Figure 14 shows that the evolution of the Stokes gain profile as a function

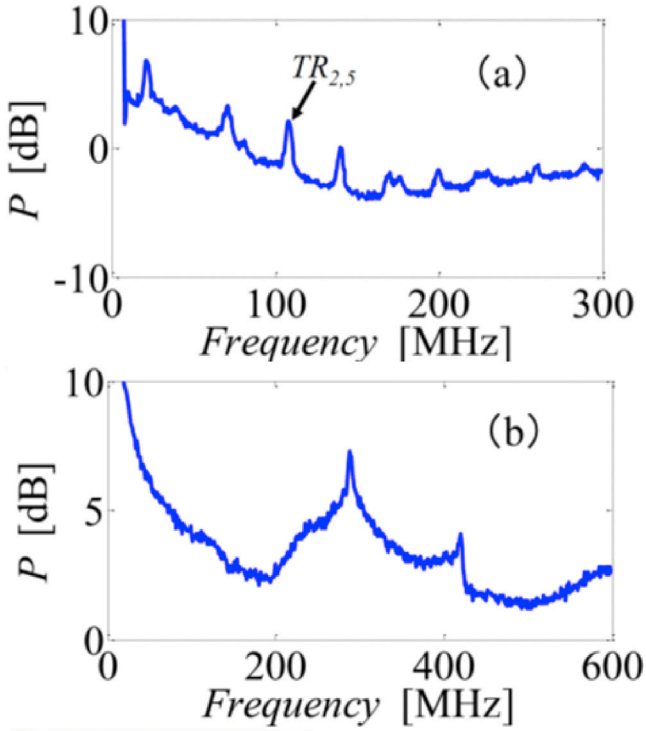

Figure 13. Experimental Results of Torsional-Radial Acoustic Modes

Measured spectra of torsional-radial acoustic modes of (A) 1.5-km-long single-mode fiber and (B) 60-cm-long As_2Se_3-PMMA fiber with As_2Se_3 diameter of 1.06 micron. Image from Gao (2019).

of pump power, and three peaks are observed. In addition to a strong stimulated Brillouin scattering at Brillouin frequency shift of 7.62 GHz and a weak one at 7.8 GHz, an amplification Stokes light at 7.4 GHz was also observed due to the modulation of guided acoustic wave Brillouin scattering.

Raman Scattering

Raman scattering in chalcogenide fibers has been investigated widely due to the large gain coefficient of chalcogenide glass and operation spectrum over the wavelength range of 1–10 μm (Bernier et al., 2013; Slusher et al., 2004). A Raman laser with a wavelength of 3.34 μm has been demonstrated based on a 3 m-long single-mode As_2S_3 fiber (Bernier et al., 2013; Slusher et al., 2004).

Microwires further enhance the nonlinear gain, in which the optical intensity is enhanced by more than two orders of magnitude due to the reduced waveguide mode area. Ahmad demonstrated the first Raman lasing based on a 13-cm-long single-core As_2Se_3-PMMA microwire with As_2Se_3 core diameter of 0.95 μm (Ahmad and Rochette, 2012c) and then they reported a Raman laser based on a single-core As_2Se_3-PMMA microwire with core diameter of 1.01 μm, in which the core diameter was chosen to operate in near zero-dispersion wavelength for the pump laser (Ahmad and Rochette, 2014). The resonant cavity of this Raman laser included two FBGs directly written in the As_2Se_3 microwire, as shown in Figure 15. Figure 16 shows that Raman lasing is observed at a wavelength of 1,585 nm as the device is pumped at different optical power at the wavelength of 1,532 nm. Four-wave mixing was also observed in this microwire-based Raman laser due to (1) large Raman and parametric gain that is up to five orders of magnitude larger than that in silica fibers and (2) precisely engineered chromatic dispersion of microwires. Abdukerim (Abdukerim et al., 2017) reported a Raman fiber laser based on a multi-material chalcogenide microwire with a core of $As_{38}Se_{62}$, a cladding of $As_{28}S_{62}$, and a PMMA coating. The core was tapered down to 0.85 μm and a Raman lasing at a wavelength of 2.025 μm occurred from a pump light at a wavelength of 1.938 μm.

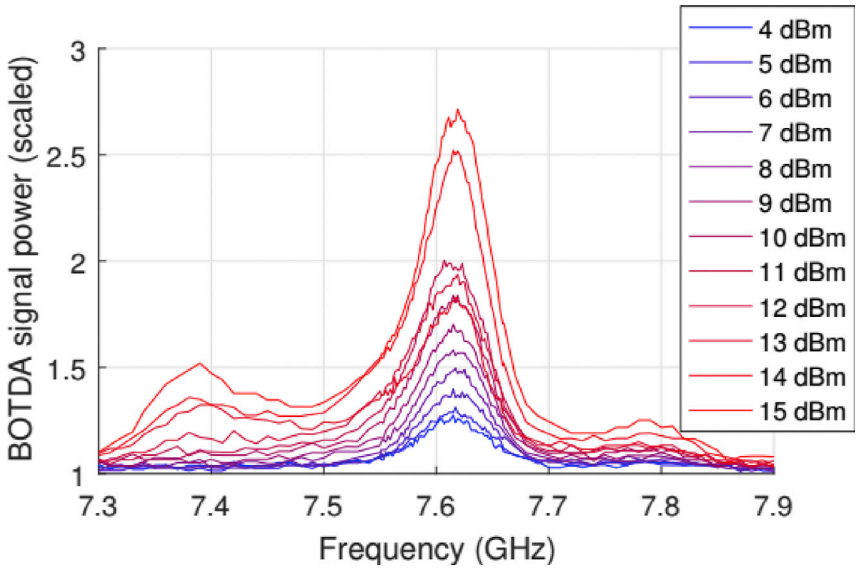

Figure 14. Evolution of the Stokes Gain Profile as a Function of Pump Power
Image from Saxena et al. (2019b).

Nonlinear Polarization-Rotation-Based Mode-Locked Laser

In a laser, each longitudinal mode oscillates independently with no fixed relationship between each other. If each mode operates with a fixed phase between it and the other modes, the laser output produces an intense burst or pulse of light, which is called mode-locked lasers. Usually, the laser resonator contains some mode-locking devices: either an active element (an optical modulator) or a nonlinear passive element (a saturable absorber) (Lamb, 1964).

Al-Kadry (Al-Kadry et al., 2015a) reported a mode-locked fiber laser using a 10-cm-long As_2S_3-PMMA taper as the nonlinear medium with a core diameter of 1.7 μm. The laser is passively mode-locked based on nonlinear polarization rotation and can be adjusted for multi-wavelength laser operation. Combination of mode-locked and multi-wavelength lasers has many applications in optical sensing and spectroscopy.

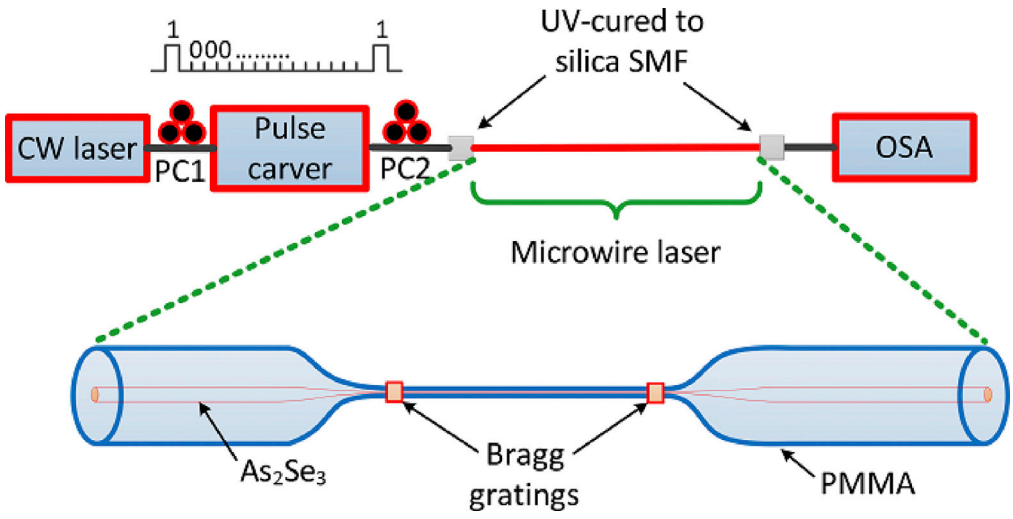

Figure 15. Raman Lasing Setup
Image from Ahmad and Rochette (2014).

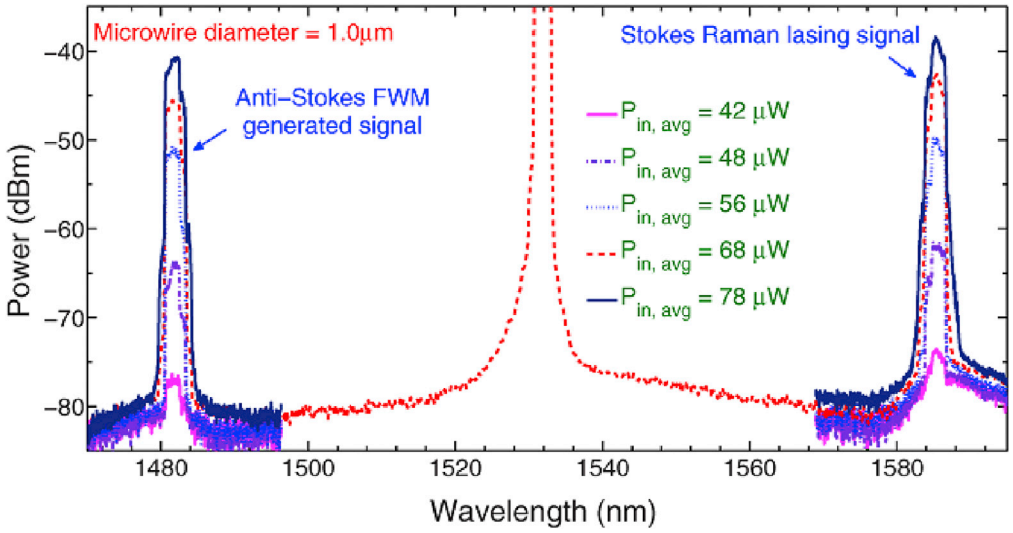

Figure 16. Output Spectra Showing the Simultaneous Operation of Raman Laser and FWM Wavelength at Different Input Pump Power Levels
Image from Ahmad and Rochette (2012c).

Supercontinuum Generation

When optical pulses propagate through highly nonlinear fibers, nonlinear effects generate new frequencies beyond the pulse spectrum so that the pulse spectrum is broadened, which is called supercontinuum generation (Agrawal, 2000). The supercontinuum is driven mainly by self-phase modulation, optical wave-breaking, stimulated Raman scattering, and four-wave mixing (Heidt et al., 2017). Supercontinuum source has many applications such as mid-IR frequency combs (Schliesser et al., 2012), molecular spectroscopy (Sanders, 2002), early cancer diagnosis (Seddon, 2013), and remote sensing (Lambert-Girard et al., 2015). Chalcogenide fibers have high nonlinearity, which is good for these nonlinear effects. However, the material dispersion of chalcogenide fibers is usually large in the normal dispersion region. Engineering dispersion can be achieved by controlling the waveguide geometry, such as tapering down the diameter of the fiber, which can make the total dispersion from normal to anomalous and greatly increase the nonlinearity of the waveguide. So chalcogenide tapers are promising devices for supercontinuum generation.

Mägi (Mägi et al., 2007) demonstrated the first As_2S_3-taper-based supercontinuum generation with spectrum broadening of 40 nm. The waist diameter was reduced to 1.2 μm and the nonlinearity is increased to 68 $W^{-1}m^{-1}$. Hudson (Hudson et al., 2011) used an As_2S_3 taper with the taper waist diameter of 1.3μm for supercontinuum generation from 970 to 1,990 nm using low pulse energy of 77 pJ.

Two-photon absorption is an unavoidable absorption process, which limits the efficiency of nonlinear effects. Figure 17A presents the two-photon absorption of As_2Se_3 as a function of normalized energy, showing it decreases as the increase of the wavelength.

As such, to avoid two-photon absorption, extending the wavelength of laser sources to long wavelength is a logical way. Al-kadry (Al-kadry et al., 2013) used an SMF shown in Figure 17B to shift the initial pump wavelength to 1,775 nm by means of Raman effect to avoid the two-photon absorption. At 1,775 nm, the group velocity dispersion β_2 is −102 ps^2/km, which is in the anomalous dispersion range. A supercontinuum generation with spectrum from 1,260 to 2,200 nm using a femtosecond (fs) pulse was observed in a 10-cm-long As_2Se_3 microwire with a core diameter of 1.28 μm. As shown in Figure 18, at a peak power of 18.8 W, the −20 dB spectrum was extended to 940 nm. Al-kadry (Al-Kadry et al., 2014) demonstrated firstly a supercontinuum generation covering two octaves of bandwidth from 1.1 μm to 4.4 μm in a 10-cm-long As_2Se_3 microwire. The core diameter is optimized to 1.6 μm to locate the pump wavelength in the anomalous dispersion regime with β_2= −130 ps^2/km and γ = 32.2 $W^{-1}m^{-1}$, which realizes the 3.3-μm-broad bandwidth using low pump pulse energy of 500 pJ. Al-kadry (Al-Kadry et al., 2015b) also introduced a supercontinuum generation in the normal dispersion regime. A 3-mm-long As_2S_3-PMMA microwire was

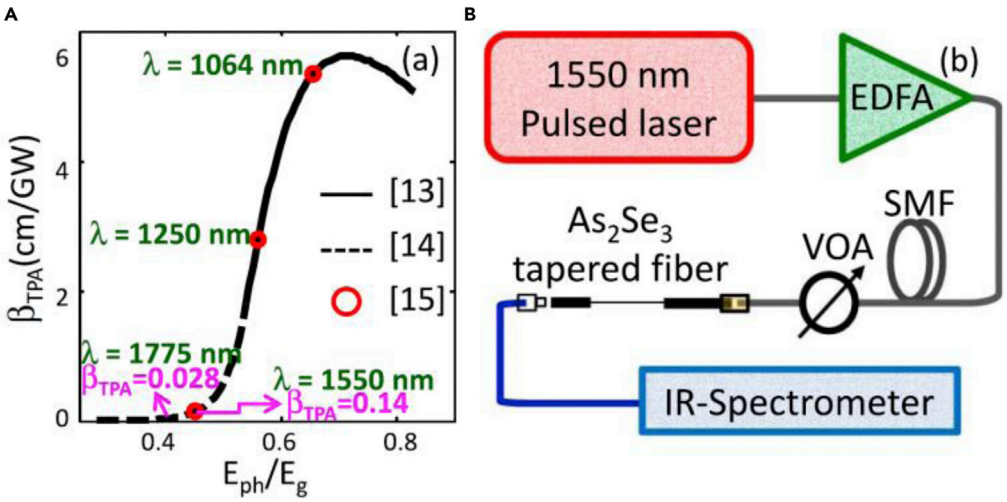

Figure 17. Experimental Study on Supercontinuum Generation

(A) Two-photon absorption spectrum of As_2Se_3 as a function of normalized energy.

(B) Experimental setup for supercontinuum generation. Image from Al-kadry et al. (2013).

tapered down to a diameter of 0.58 μm for supercontinuum generation from 960 to 2,500 nm using low pulse energy of 150 pJ. Instead of soliton fission used in the anomalous dispersion regime, it is based on optical wave breaking to achieve a broad supercontinuum generation (Hasegawa and Tappert, 1973). The PMMA coating contributes to achieving the normal dispersion and also low power consumption for supercontinuum generation, which is not achievable in air coating tapers.

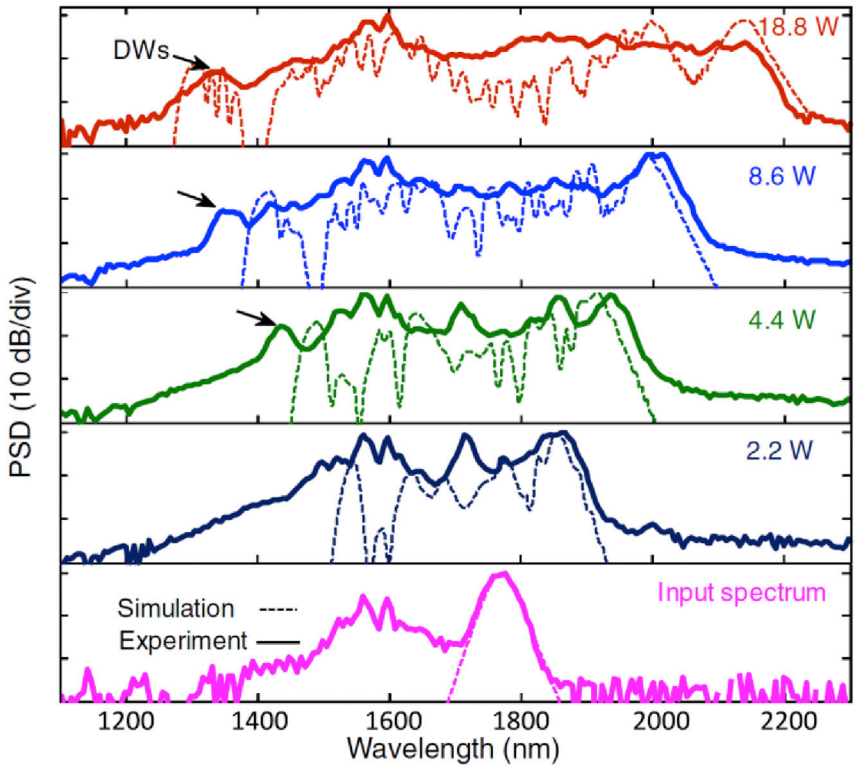

Figure 18. Supercontinuum Generation Measured as the Increase of Pump Power

Image from Al-kadry et al. (2013).

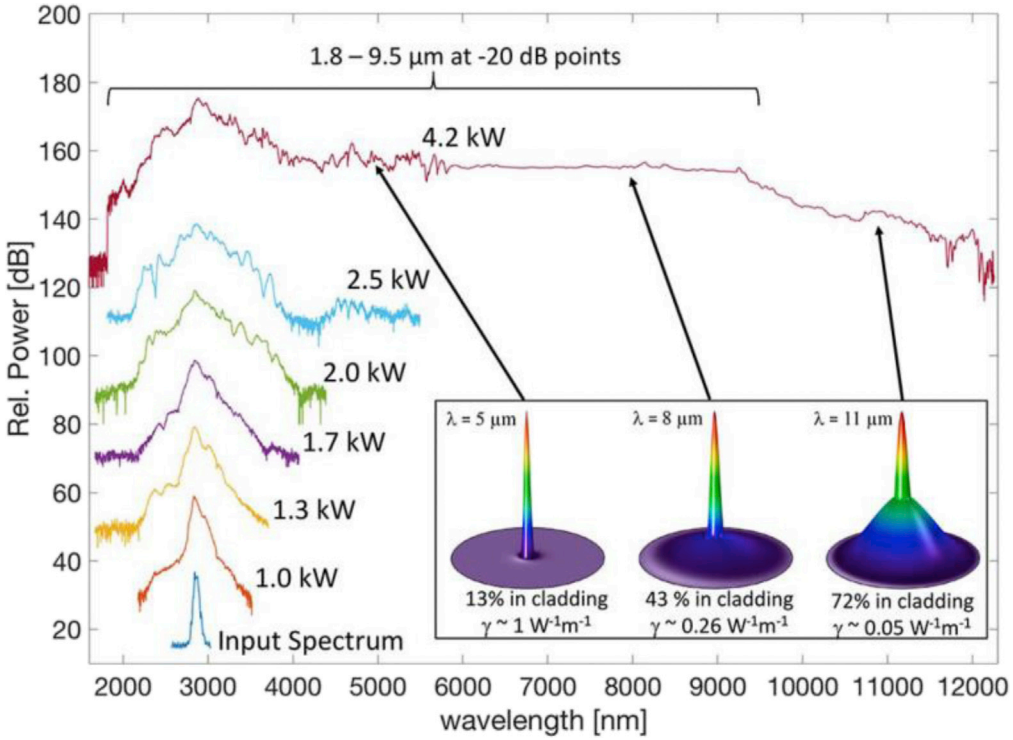

Figure 19. Spectral Expansion as the Increase of Peak Power
Image from Hudson et al. (2017).

Sun (Sun et al., 2015) tapered down the diameter of an As_2Se_3-As_2S_3 fiber to 1.9 μm for supercontinuum generation. The pumping pulses with a pulse duration of 100 fs was set at the wavelength of 3.4 μm (the zero dispersion wavelength of the taper was shifted to 3.3 μm at the diameter of 1.9 μm), and the generated supercontinuum spanned from a wavelength of 1.5 μm–4.8 μm.

Hudson (Hudson et al., 2017) reported a supercontinuum generation by a pulse laser at 2.9 μm with a pulse duration of 230 fs and peak power of 4.2 kW based on a 5-cm-long As_2Se_3-As_2S_3-PMMA fiber with As_2Se_3 core diameter of 3 μm. Figure 19 shows the evolution of spectrum as the increase of peak power. As the peak power increased to 4.2 kW, the supercontinuum spectrum was broadened to 12 μm.

SENSING APPLICATIONS

In this section, we will review As_2Se_3-PMMA tapers for sensing applications in

- Simultaneous temperature and strain measurement
- Techniques for sensitivity enhancement for temperature and strain measurement
- Temperature-insensitive strain sensor
- Transverse strain measurement
- Ultrasound measurement

Simultaneous Temperature and Strain Measurement

Gao (Gao et al., 2017) demonstrated an approach for simultaneous temperature and strain measurement in a dual-core As_2Se_3-PMMA taper with As_2Se_3 core diameter of 0.55 μm. Measurement was done by observing the two troughs from the transmission spectra of two axes when temperature and strain were changed. Measurement sensitivities are calculated for both principal polarization axes with temperature sensitivities of −115 pm/°C for axis-1 and −35.5 pm/°C for axis-2 and strain sensitivities of −4.21 pm/με for axis-1 and −3.16 pm/με for axis-2.

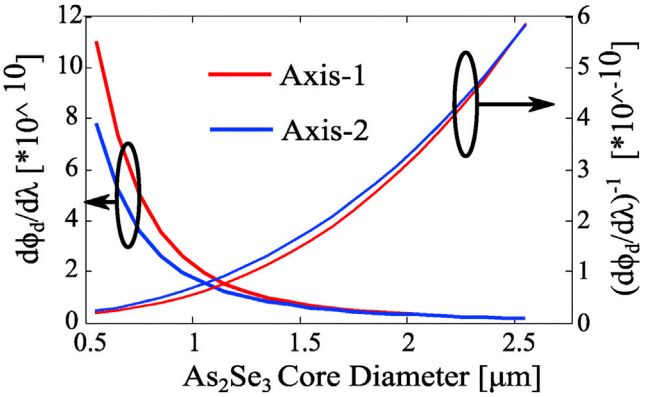

Figure 20. Calculated Values of $\partial\varphi_d/\partial\lambda$ and $(\partial\varphi_d/\partial\lambda)^{-1}$ as a Function of As_2Se_3 Core Diameter
Image from Gao et al. (2018b).

Techniques for Sensitivity Enhancement for Temperature and Strain Measurement

To enhance the temperature and strain sensitivity in dual-core As_2Se_3-PMMA tapers, two approaches have been investigated (Gao et al., 2018b, 2019b). The wavelength shift of troughs in the transmission spectrum is proportional to the value of the variation of the difference between phases of the even and odd modes with respect to wavelength ($\partial\varphi_d(\lambda)/\partial\lambda$) (Gao et al., 2017). So the basic principle is to reduce the value of $\partial\varphi_d(\lambda)/\partial\lambda$. The first approach is by increasing the diameter of As_2Se_3 core and PMMA cladding to reduce the value of $\partial\varphi_d(\lambda)/\partial\lambda$ and to increase thermal forces in a dual-core As_2Se_3-PMMA taper (Gao et al., 2018b). As shown in Figure 20, the value of $\partial\varphi_d(\lambda)/\partial\lambda$ decreases as the As_2Se_3 core diameter increases. Thermal forces on the As_2Se_3 cores induced by the large difference of thermal expansion coefficients between As_2Se_3 cores and PMMA cladding are also enhanced by PMMA cladding with large diameters (Gao et al., 2018a). These two effects work together to enhance the measurement sensitivity. A fiber with As_2Se_3 core diameter of 2.5 μm was tested, and the sensitivities are 436 pm/°C and −6.23 pm/με and 572 pm/°C and −3.63 pm/με from the transmission spectra of axis-1 and axis-2, respectively.

The second approach is based on effective group-velocity matching between the even and odd modes of a dual-core As_2Se_3-PMMA taper on which an antisymmetric long-period grating is inscribed (Gao et al., 2019b). The variation of the difference between phases of the even and odd modes with respect to wavelength tends to 0 ($\partial\varphi_d(\lambda)/\partial\lambda \rightarrow 0$) near the resonance wavelength of the grating due to the effective group-velocity matching between the two modes, and consequently, thermally induced change of the difference between phases of the two modes $\varphi_d(\lambda)$ leads to a large wavelength shift indicating enhancement of the temperature measurement sensitivity. As shown in Figure 21, temperature measurement sensitivity enhancement by a factor of 4.0 is achieved in comparison with the sensitivity in the wavelength range

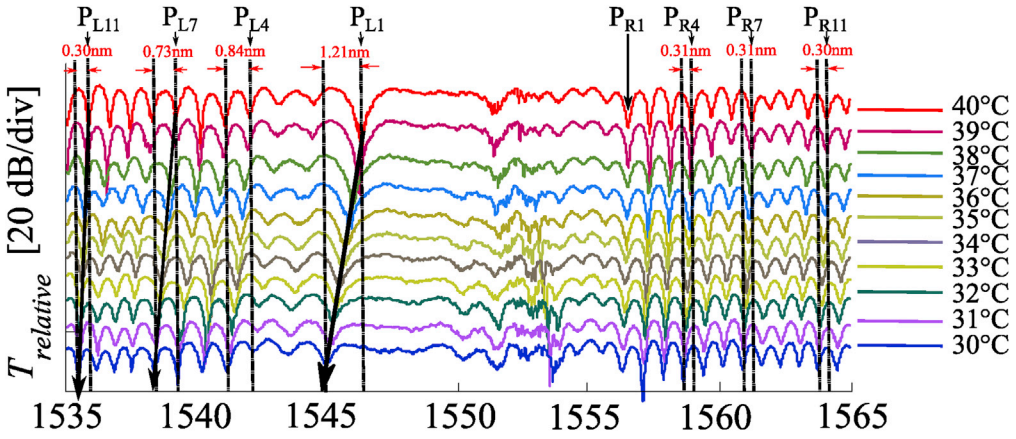

Figure 21. Evolution of Measured Transmission Spectrum as a Function of Temperature
Image from Gao et al. (2019b).

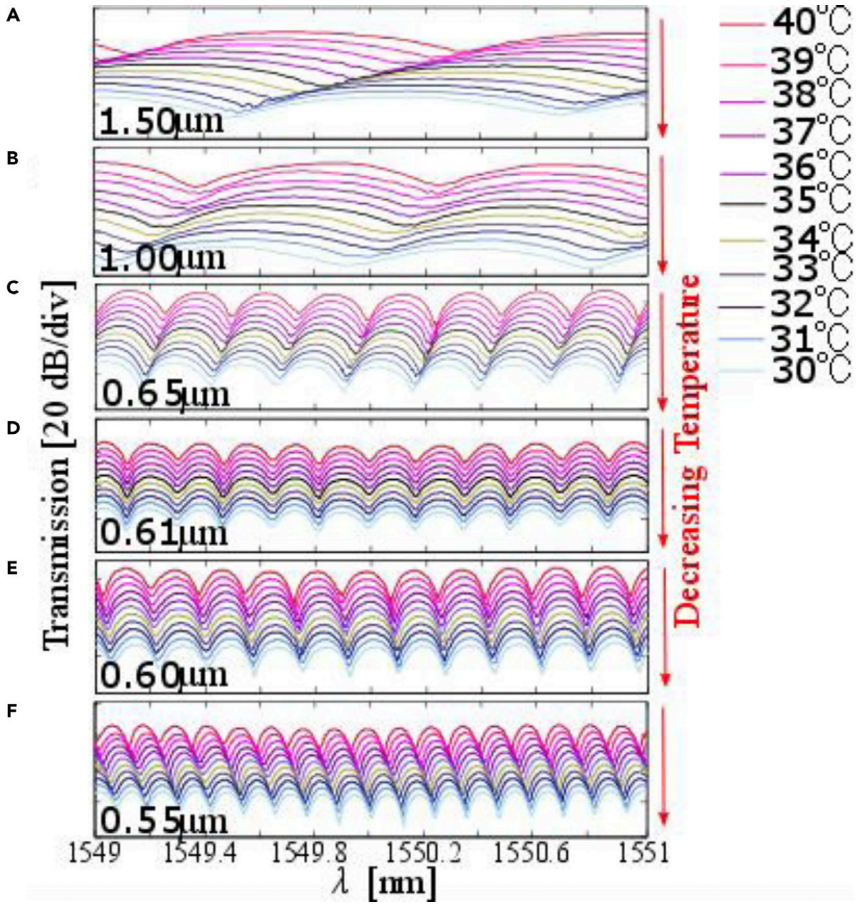

Figure 22. Experimental Results of Temperature Measurement

Evolution of the transmission spectra of the six tapered dual-core As_2Se_3-PMMA fibers with As_2Se_3 core diameters of (A) 1.50 μm, (B) 1.00 μm, (C) 0.65 μm, (D) 0.61 μm, (E) 0.60 μm, and (F) 0.55 μm as the temperature decreases (Δ T<0). Image from Gao et al. (2018a).

that does not have effective group velocity matching in the dual-core taper with As_2Se_3 core diameter of 1.5 μm.

Temperature-Insensitive Strain Sensor

The thermal forces in a dual-core As_2Se_3-PMMA taper are investigated (Gao et al., 2018a). The thermal expansion coefficient of PMMA is up to 10 times larger than that of As_2Se_3, which induces longitudinal and transverse forces on the As_2Se_3 cores by thermal expansion/contraction of the PMMA cladding. The temperature-insensitive condition is achieved at an optimal PMMA layer thickness by the counterbalance of the wavelength shift caused by the thermally induced forces on the refractive index of the dual-core fiber cores and that caused by the thermally induced fiber length variation. A temperature-insensitive strain sensor is proposed and demonstrated based on the thermal forces in a dual-core As_2Se_3-PMMA fiber with an As_2Se_3 core diameter of 0.61 μm and a PMMA cladding diameter of 34.4 μm, which is shown in Figure 22.

Transverse Strain Sensing

Saxena (Saxena et al., 2019a) reported calibration of transverse load based on the Brillouin frequency shift in a 60 cm As_2Se_3-PMMA taper with a sensitivity of 0.08 MHz/N. The diameters of As_2Se_3 core and PMMA cladding are 2 μm and 100 μm, respectively. Figure 23 presents the experimental results showing the Brillouin frequency spectrum shifts from 0 (blue) to a 4 kg load (red) at 1 kg increment.

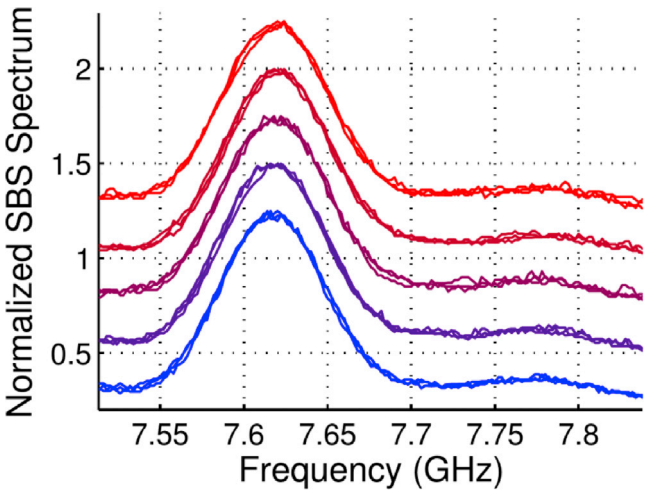

Figure 23. Experimental Results of the Brillouin Frequency Spectrum as the Load from 0 (Blue) to a 4 kg Load (Red) at 1 kg Increment

Ultrasound Measurement

Gao (Gao et al., 2019a) demonstrated an ultrasound sensor based on a dual-core As_2Se_3-PMMA taper with a Young's modulus 24 times smaller than that of silica fibers. Due to the dual-core structure, low Young's modulus, sub-micrometer dimension of core, and the high-contrast interference pattern by the even and odd modes, this ultrasound sensor shows high sensitivities to both shear and longitudinal waves of ultrasound waves in the frequency range from 10 kHz to 34 MHz.

Conclusion and Outlook

Chalcogenide tapers and their applications have been reviewed in this work, which highlights the main features and emerging trends. This review mainly focuses on the various applications by different nonlinear effects and sensing applications in the chalcogenide tapers due to the high nonlinear coefficient and engineered dispersion.

Tapered chalcogenide-polymer fibers composed of chalcogenide cores and a polymer material as cladding are promising platforms for sensing and nonlinear applications. The polymer cladding/coating provides high robustness, high flexibility, and ease of handing, which has great advantages over the silica fibers (Peters, 2010; Webb, 2015). However, the water-absorption property of the polymer is an essential factor that one should take care of when polymer materials are used in fiber sensing and nonlinear applications. Polymers as cladding or coating materials will stretch chalcogenide cores due to the absorption of water, which on the other hand can lead to humidity sensors (Zhang et al., 2010).

The inscription of FBGs and antisymmetric LPGs in single-core and dual-core As_2Se_3-PMMA tapers can lead to the realization of many mid-IR devices that are very important for mid-IR lasers and gas spectrum measurement. Antisymmetric LPGs are shown to have the potential for achieving slow light. This slow light feature can be utilized for the implementation of highly sensitive devices for the measurement of temperature and refractive-index change of a liquid solution.

Nonlinear effects and sensing applications in chalcogenide tapers bring out many promising applications in mid-IR sensing, lasers, and spectroscopy. It will open the path toward the realization of many practical and encouraging applications and fundamental research.

ACKNOWLEDGMENTS

This work was supported by NSERC Discovery Grant (06071-RGPIN-2015) and Canada Research Chair, CRC, in Fiber Optics and Photonics Program (75-67138).

AUTHOR CONTRIBUTIONS

S.G. wrote and edited this review article. X. B. revised it.

REFERENCES

Abdukerim, N., Li, L., El Amraoui, M., Messaddeq, Y., and Rochette, M. (2017). 2 μ m Raman fiber laser based on a multimaterial chalcogenide microwire. Appl. Phys. Lett. *110*, 161103.

Abdukerim, N., Li, L., and Rochette, M. (2016). Chalcogenide-based optical parametric oscillator at 2 μm. Opt. Lett. *41*, 4364–4367.

Abedin, K.S. (2005). Observation of strong stimulated Brillouin scattering in single-mode As 2 Se 3 chalcogenide fiber. Optic. Express *13*, 10266–10271.

Afshar, S., and Monro, T.M. (2009). A full vectorial model for pulse propagation in emerging waveguides with subwavelength structures part I: Kerr nonlinearity. Optic. Express *17*, 2298–2318.

Agrawal, G.P. (1987). Modulation instability induced by cross-phase modulation. Phys. Rev. Lett. *59*, 880.

Agrawal, G.P. (2000). Nonlinear fiber optics. In Nonlinear Science at the Dawn of the 21st Century (Springer), pp. 195–211.

Ahmad, R., and Rochette, M. (2011). Photosensitivity at 1550 nm and Bragg grating inscription in As2Se3 chalcogenide microwires. Appl. Phys. Lett. *99*, 061109.

Ahmad, R., and Rochette, M. (2012a). Chalcogenide optical parametric oscillator. Optic. Express *20*, 10095–10099.

Ahmad, R., and Rochette, M. (2012b). High efficiency and ultra broadband optical parametric four-wave mixing in chalcogenide-PMMA hybrid microwires. Optic. Express *20*, 9572–9580.

Ahmad, R., and Rochette, M. (2012c). Raman lasing in a chalcogenide microwire-based Fabry–Perot cavity. Opt. Lett. *37*, 4549–4551.

Ahmad, R., and Rochette, M. (2014). All-chalcogenide Raman-parametric laser, wavelength converter, and amplifier in a single microwire. IEEE J. Sel. Top. Quant. Electron. *20*, 299–304.

Ahmad, R., Rochette, M., and Baker, C. (2011). Fabrication of Bragg gratings in subwavelength diameter As 2 Se 3 chalcogenide wires. Opt. Lett. *36*, 2886–2888.

Al-kadry, A., Baker, C., El Amraoui, M., Messaddeq, Y., and Rochette, M. (2013). Broadband supercontinuum generation in As 2 Se 3 chalcogenide wires by avoiding the two-photon absorption effects. Opt. Lett. *38*, 1185–1187.

Al-Kadry, A., El Amraoui, M., Messaddeq, Y., and Rochette, M. (2014). Two octaves mid-infrared supercontinuum generation in As 2 Se 3 microwires. Optic. Express *22*, 31131–31137.

Al-Kadry, A., El Amraoui, M., Messaddeq, Y., and Rochette, M. (2015a). Mode-locked fiber laser based on chalcogenide microwires. Opt. Lett. *40*, 4309–4312.

Al-Kadry, A., Li, L., El Amraoui, M., North, T., Messaddeq, Y., and Rochette, M. (2015b). Broadband supercontinuum generation in all-normal dispersion chalcogenide microwires. Opt. Lett. *40*, 4687–4690.

Alamgir, I., Abdukerim, N., and Rochette, M. (2019). In situ fabrication of far-detuned optical fiber wavelength converters. Opt. Lett. *44*, 4467–4470.

Antman, Y., Clain, A., London, Y., and Zadok, A. (2016). Optomechanical sensing of liquids outside standard fibers using forward stimulated Brillouin scattering. Optica *3*, 510–516.

Asobe, M. (1997). Nonlinear optical properties of chalcogenide glass fibers and their application to all-optical switching. Opt. Fiber Tech. *3*, 142–148.

Asobe, M., Kanamori, T., and Kubodera, K.I. (1993). Applications of highly nonlinear chalcogenide glass fibers in ultrafast all-optical switches. IEEE J. Quant. Electron. *29*, 2325–2333.

Auld, B.A. (1973). Acoustic Fields and Waves in Solids (**РиЦол Классик**) (John Wiley & Sons). https://books.google.co.in/books?id=_2MWAwAAQBAJ&printsec=frontcover&dq=Acoustic+Fields+and+Waves+in+Solids+(%D0%A0%D0%B8%D0%BF%D0%BE%D0%BB+%D0%9A%D0%BB%D0%B0%D1%81%D1%81%D0%B8%D0%BA)&hl=en&sa=X&ved=0ahUKEwicn_Wt9fDmAhWTwjgGHdt_CmUQ6AEIKDAA#v=onepage&q=Acoustic%20Fields%20and%20Waves%20in%20Solids%20(%D0%A0%D0%B8%D0%BF%D0%BE%D0%BB%20%D0%9A%D0%BB%D0%B0%D1%81%D1%81%D0%B8%D0%BA)&f=false.

Baker, C. (2013). Hybrid As2Se3-PMMA Microtapers and Applications (McGill University Libraries).

Baker, C., Gao, S., Chen, L., and Bao, X. (2017). Self-inscribed antisymmetric long-period grating in a dual-core As 2 Se 3-PMMA fiber. Optic. Express *25*, 12409–12414.

Baker, C., and Rochette, M. (2010). Highly nonlinear hybrid AsSe-PMMA microtapers. Optic. Express *18*, 12391–12398.

Baker, C., and Rochette, M. (2011). A generalized heat-brush approach for precise control of the waist profile in fiber tapers. Opt. Mater. Express *1*, 1065–1076.

Baker, C., and Rochette, M. (2012). High nonlinearity and single-mode transmission in tapered multimode $\hbox {As} _ {2}\hbox {Se} _ {3} $-PMMA fibers. IEEE Photonics J. *4*, 960–969.

Bernier, M., Fortin, V., Caron, N., El-Amraoui, M., Messaddeq, Y., and Vallée, R. (2013). Mid-infrared chalcogenide glass Raman fiber laser. Opt. Lett. *38*, 127–129.

Beugnot, J.-C., Ahmad, R., Rochette, M., Laude, V., Maillotte, H., and Sylvestre, T. (2014). Reduction and control of stimulated Brillouin scattering in polymer-coated chalcogenide optical microwires. Opt. Lett. *39*, 482–485.

Birks, T., Wadsworth, W., and Russell, P.S.J. (2000). Supercontinuum generation in tapered fibers. Opt. Lett. *25*, 1415–1417.

Birks, T.A., and Li, Y.W. (1992). The shape of fiber tapers. J. Lightwave Tech. *10*, 432–438.

Biryukov, A., Sukharev, M.E.E., and Dianov, E.M. (2002). Excitation of sound waves upon propagation of laser pulses in optical fibres. Quant. Electron. *32*, 765.

Boudebs, G., Cherukulappurath, S., Guignard, M., Troles, J., Smektala, F., and Sanchez, F. (2004). Linear optical characterization of chalcogenide glasses. Opt. Commun. *230*, 331–336.

Boyd, R.W. (2011). Material slow light and structural slow light: similarities and differences for nonlinear optics. J. Opt. Soc. Am. B *28*, A38–A44.

Brambilla, G. (2010). Optical fibre nanowires and microwires: a review. J. Optic. *12*, 043001.

Brambilla, G., Xu, F., Horak, P., Jung, Y., Koizumi, F., Sessions, N.P., Koukharenko, E., Feng, X., Murugan, G.S., and Wilkinson, J.S. (2009). Optical fiber nanowires and microwires: fabrication and applications. Adv. Opt. Photon. *1*, 107–161.

Chiang, K.S. (1997a). Coupled-mode equations for pulse switching in parallel waveguides. IEEE J. Quant. Electron. *33*, 950–954.

Chiang, K.S. (1997b). Propagation of short optical pulses in directional couplers with Kerr nonlinearity. J. Opt. Soc. Am. B *14*, 1437–1443.

Dai, S., Wang, Y., Peng, X., Zhang, P., Wang, X., and Xu, Y. (2018). A review of mid-infrared supercontinuum generation in chalcogenide glass fibers. Appl. Sci. *8*, 2076–3417.

Dantanarayana, H.G., Abdel-Moneim, N., Tang, Z., Sojka, L., Sujecki, S., Furniss, D., Seddon, A.B., Kubat, I., Bang, O., and Benson, T.M. (2014). Refractive index dispersion of chalcogenide glasses for ultra-high numerical-aperture fiber for mid-infrared supercontinuum generation. Opt. Mater. Express *4*, 1444–1455.

Eggleton, B.J., Luther-Davies, B., and Richardson, K. (2011). Chalcogenide photonics. Nat. Photon. *5*, 141.

Emiliyanov, G., Jensen, J.B., Bang, O., Hoiby, P.E., Pedersen, L.H., Kjær, E.M., and Lindvold, L. (2006). Localized biosensing with Topas microstructured polymer optical fiber. Paper presented at: Optical Fiber Sensors (Optical Society of America).

Engan, H.E., Kim, B.Y., Blake, J.N., and Shaw, H.J. (1988). Propagation and optical interaction of guided acoustic waves in two-mode optical fibers. J. Lightwave Tech. *6*, 428–436.

Florea, C., Sanghera, J., Shaw, B., and Aggarwal, I. (2009). Fiber Bragg gratings in As2S3 fibers obtained using a 0/− 1 phase mask. Opt. Mater. *31*, 942–944.

Fu, L., Rochette, M., Ta'eed, V., Moss, D., and Eggleton, B. (2005). Investigation of self-phase modulation based optical regeneration in single mode As 2 Se 3 chalcogenide glass fiber. Optic. Express *13*, 7637–7644.

Gao, S. (2019). Fabrication of Tapered Dual-Core As2Se3-PMMA Fiber and Its Applications (Université d'Ottawa/University of Ottawa).

Gao, S., Baker, C., Cai, W., Chen, L., and Bao, X. (2019a). 10 kHz-34 MHz ultrasound detection based on a dual-core hybrid taper. APL Photon. *4*, 110805.

Gao, S., Baker, C., Chen, L., and Bao, X. (2017). Simultaneous measurement of temperature and strain in a dual-core As 2 Se 3-PMMA taper. IEEE Photonics Technol. Lett. *30*, 79–82.

Gao, S., Baker, C., Chen, L., and Bao, X. (2018a). Approach for temperature-insensitive strain measurement using a dual-core as 2 Se 3-PMMA taper. Opt. Lett. *43*, 1523–1526.

Gao, S., Baker, C., Chen, L., and Bao, X. (2018b). High-sensitivity temperature and strain measurement in dual-core hybrid tapers. IEEE Photonics Technol. Lett. *30*, 1155–1158.

Gao, S., Baker, C., Chen, L., and Bao, X. (2019b). Approach for temperature-sensitivity enhancement in a tapered dual-core as 2 Se 3-PMMA fiber with an antisymmetric long-period grating. J. Lightwave Tech. *37*, 2734–2738.

Gattass, R.R., Svacha, G.T., Tong, L., and Mazur, E. (2006). Supercontinuum generation in submicrometer diameter silica fibers. Optic. Express *14*, 9408–9414.

Godin, T., Combes, Y., Ahmad, R., Rochette, M., Sylvestre, T., and Dudley, J.M. (2014). Far-detuned mid-infrared frequency conversion via normal dispersion modulation instability in chalcogenide microwires. Opt. Lett. *39*, 1885–1888.

Harrington, J.A. (2004). Infrared fiber optics (SPIE).

Harvey, J.D., Leonhardt, R., Coen, S., Wong, G.K., Knight, J., Wadsworth, W.J., and Russell, P.S.J. (2003). Scalar modulation instability in the normal dispersion regime by use of a photonic crystal fiber. Opt. Lett. *28*, 2225–2227.

Hasegawa, A., and Tappert, F. (1973). Transmission of stationary nonlinear optical pulses in dispersive dielectric fibers. I. Anomalous dispersion. Appl. Phys. Lett. *23*, 142–144.

Hayashi, N., Mizuno, Y., Koyama, D., and Nakamura, K. (2011). Measurement of acoustic velocity in poly (methyl methacrylate)-based polymer optical fiber for Brillouin frequency shift estimation. Appl. Phys. Express *4*, 102501.

Hayashi, N., Mizuno, Y., Nakamura, K., Set, S.Y., and Yamashita, S. (2017). Experimental study on depolarized GAWBS spectrum for optomechanical sensing of liquids outside standard fibers. Optic. Express *25*, 2239–2244.

Heidt, A.M., Feehan, J.S., Price, J.H., and Feurer, T. (2017). Limits of coherent supercontinuum generation in normal dispersion fibers. J. Opt. Soc. Am. B *34*, 764–775.

Hudson, D.D., Antipov, S., Li, L., Alamgir, I., Hu, T., El Amraoui, M., Messaddeq, Y., Rochette, M., Jackson, S.D., and Fuerbach, A. (2017). Toward all-fiber supercontinuum spanning the mid-infrared. Optica *4*, 1163–1166.

Hudson, D.D., Dekker, S.A., Mägi, E.C., Judge, A.C., Jackson, S.D., Li, E., Sanghera, J., Shaw, L., Aggarwal, I., and Eggleton, B.J. (2011). Octave spanning supercontinuum in an As 2 S 3 taper using ultralow pump pulse energy. Opt. Lett. *36*, 1122–1124.

Humbach, O., Fabian, H., Grzesik, U., Haken, U., and Heitmann, W. (1996). Analysis of OH absorption bands in synthetic silica. J. Non Cryst. Solids *203*, 19–26.

Jarschel, P., Magalhaes, L., Aldaya, I., Florez, O., and Dainese, P. (2018). Fiber taper diameter characterization using forward Brillouin scattering. Opt. Lett. *43*, 995–998.

Jensen, J.B., Hoiby, P.E., Emiliyanov, G., Bang, O., Pedersen, L.H., and Bjarklev, A. (2005). Selective detection of antibodies in microstructured polymer optical fibers. Optic. Express *13*, 5883–5889.

Kanamori, T., Terunuma, Y., and Miyashita, T. (1984). Preparation of chalcogenide optical fiber. Rev. Electr. Commun. Lab. *32*, 469–477.

Kanellos, G.T., Papaioannou, G., Tsiokos, D., Mitrogiannis, C., Nianios, G., and Pleros, N. (2010). Two dimensional polymer-embedded quasi-distributed FBG pressure sensor for biomedical applications. Optic. Express *18*, 179–186.

Kang, M., Nazarkin, A., Brenn, A., and Russell, P.S.J. (2009). Tightly trapped acoustic phonons in photonic crystal fibres as highly nonlinear artificial Raman oscillators. Nat. Phys. *5*, 276.

Kenny, R., Birks, T., and Oakley, K. (1991). Control of optical fibre taper shape. Electron. Lett. *27*, 1654–1656.

Kersey, A.D., Berkoff, T., and Morey, W. (1993). Multiplexed fiber Bragg grating strain-sensor system with a fiber Fabry–Perot wavelength filter. Opt. Lett. *18*, 1370–1372.

Kim, K., Stolen, R., Reed, W., and Quoi, K. (1994). Measurement of the nonlinear index of silica-core and dispersion-shifted fibers. Opt. Lett. *19*, 257–259.

Kitamura, R., Pilon, L., and Jonasz, M. (2007). Optical constants of silica glass from extreme ultraviolet to far infrared at near room temperature. Appl. Opt. *46*, 8118–8133.

Kuzyk, M.G. (2018). Polymer Fiber Optics: Materials, Physics, and Applications (CRC press).

Lamb, W.E., Jr. (1964). Theory of an optical maser. Phys. Rev. *134*, A1429.

Lambert-Girard, S., Allard, M., Piché, M., and Babin, F. (2015). Differential optical absorption spectroscopy lidar for mid-infrared gaseous measurements. Appl. Opt. *54*, 1647–1656.

Lamont, M.R., Luther-Davies, B., Choi, D.-Y., Madden, S., Gai, X., and Eggleton, B.J. (2008). Net-gain from a parametric amplifier on a chalcogenide optical chip. Optic. Express *16*, 20374–20381.

Le, S.D., Gay, M., Bramerie, L., e Silva, M.C., Lenglé, K., Chartier, T., Thual, M., Simon, J.-C., Brilland, L., and Méchin, D. (2012). Wavelength conversion in a highly nonlinear chalcogenide microstructured fiber. Opt. Lett. *37*, 4576–4578.

Lee, H., and Agrawal, G.P. (2003). Nonlinear switching of optical pulses in fiber Bragg gratings. IEEE J. Quant. Electron. *39*, 508–515.

Letokhov, V. (1968). Generation of light by a scattering medium with negative resonance absorption. Sov. Phys. JETP *26*, 835–840.

Li, J.H., Chiang, K.S., and Chow, K.W. (2011). Modulation instabilities in two-core optical fibers. J. Opt. Soc. Am. B *28*, 1693–1701.

Li, L., Abdukerim, N., and Rochette, M. (2016a). Chalcogenide optical microwires cladded with fluorine-based CYTOP. Optic. Express *24*, 18931–18937.

Li, L., Abdukerim, N., and Rochette, M. (2017). Mid-infrared wavelength conversion from as 2 Se 3 microwires. Opt. Lett. *42*, 639–642.

Li, L., Al-Kadry, A., Abdukerim, N., and Rochette, M. (2016b). Design, fabrication and characterization of PC, COP and PMMA-cladded as 2 Se 3 microwires. Opt. Mater. Express *6*, 912–921.

Li, T. (2012). Optical Fiber Communications: Fiber Fabrication (Elsevier).

Mägi, E.C., Fu, L., Nguyen, H.C., Lamont, M., Yeom, D., and Eggleton, B. (2007). Enhanced Kerr nonlinearity in sub-wavelength diameter As2Se3 chalcogenide fiber tapers. Optic. Express *15*, 10324–10329.

Miya, T., Terunuma, Y., Hosaka, T., and Miyashita, T. (1979). Ultimate low-loss single-mode fibre at 1.55 μm. Electron. Lett. *15*, 106–108.

Miyashita, T., and Terunuma, Y. (1982). Optical transmission loss of as–S glass fiber in 1.0–5.5 μm wavelength region. Jpn. J. Appl. Phys. *21*, L75.

Peral, E., and Yariv, A. (1999). Degradation of modulation and noise characteristics of semiconductor lasers after propagation in optical fiber due to a phase shift induced by stimulated Brillouin scattering. IEEE J. Quant. Electron. *35*, 1185–1195.

Peters, K. (2010). Polymer optical fiber sensors—a review. Smart Mater. Struct. *20*, 013002.

Petropoulos, P., Ibsen, M., Ellis, A., and Richardson, D.J. (2001). Rectangular pulse generation based on pulse reshaping using a superstructuredfiber bragg grating. J. Lightwave Tech. *19*, 746.

Pitois, S., and Millot, G. (2003). Experimental observation of a new modulational instability spectral window induced by fourth-order dispersion in a normally dispersive single-mode optical fiber. Opt. Commun. *226*, 415–422.

Rochette, M. and Baker, C. (2014). Highly nonlinear optical waveguide structure with enhanced nonlinearity and mechanical robustness (Google Patents).

Rodney, W.S., Malitson, I.H., and King, T.A. (1958). Refractive index of arsenic trisulfide. J. Opt. Soc. Am. *48*, 633–636.

Rothenberg, J.E. (1990). Modulational instability for normal dispersion. Phys. Rev. A *42*, 682.

Russell, P.S.J., Culverhouse, D., and Farahi, F. (1990). Experimental observation of forward stimulated Brillouin scattering in dual-mode single-core fibre. Electron. Lett. *26*, 1195–1196.

Russell, P.S.J., Culverhouse, D., and Farahi, F. (1991). Theory of forward stimulated Brillouin scattering in dual-mode single-core fibers. IEEE J. Quant. Electron. *27*, 836–842.

Sanders, S. (2002). Wavelength-agile fiber laser using group-velocity dispersion of pulsed supercontinua and application to broadband absorption spectroscopy. Appl. Phys. B *75*, 799–802.

Sanghera, J., Aggarwal, I., Shaw, L., Busse, L., Thielen, P., Nguyen, V., Pureza, P., Bayya, S., and Kung, F. (2001). Applications of chalcogenide glass optical fibers at NRL. J. Optoelectron. Adv. Mater. *3*, 627–640.

Sanghera, J.S., Shaw, L.B., and Aggarwal, I.D. (2002). Applications of chalcogenide glass optical fibers. Compt. Rendus Chem. *5*, 873–883.

Sanghera, J.S., Shaw, L.B., and Aggarwal, I.D. (2009). Chalcogenide glass-fiber-based mid-IR sources and applications. IEEE J. Sel. Top. Quant. Electron. *15*, 114–119.

Sanghera, J.S., Shaw, L.B., Pureza, P., Nguyen, V.Q., Gibson, D., Busse, L., Aggarwal, I.D., Florea, C.M., and Kung, F.H. (2010). Nonlinear properties of chalcogenide glass fibers. Int. J. Appl. Glass Sci. *1*, 296–308.

Saxena, B., Baker, C., Bao, X., and Chen, L. (2019a). High birefringent Brillouin frequency shifts in a single-mode as 2 Se 3-PMMA microtaper induced by a transverse load. Opt. Lett. *44*, 4789–4792.

Saxena, B., Baker, C., Bao, X., and Chen, L. (2019b). Simultaneous generation of guided-acoustic-wave Brillouin scattering and stimulated-Brillouin-scattering in hybrid as 2 Se 3-PMMA microtapers. Optic. Express *27*, 13734–13743.

Schliesser, A., Picqué, N., and Hänsch, T.W. (2012). Mid-infrared frequency combs. Nat. Photon. *6*, 440.

Seddon, A.B. (2013). Mid-infrared (IR)–A hot topic: the potential for using mid-IR light for non-invasive early detection of skin cancer in vivo. Phys. Status Solidi B *250*, 1020–1027.

Shelby, R., Levenson, M., and Bayer, P. (1985). Guided acoustic-wave Brillouin scattering. Phys. Rev. B *31*, 5244.

Silva-López, M., Fender, A., MacPherson, W.N., Barton, J.S., Jones, J.D., Zhao, D., Dobb, H., Webb, D.J., Zhang, L., and Bennion, I. (2005). Strain and temperature sensitivity of a single-mode polymer optical fiber. Opt. Lett. *30*, 3129–3131.

Slusher, R.E., Lenz, G., Hodelin, J., Sanghera, J., Shaw, L.B., and Aggarwal, I.D. (2004). Large Raman gain and nonlinear phase shifts in high-purity as 2 Se 3 chalcogenide fibers. JOSA B *21*, 1146–1155.

Song, K.Y., Abedin, K.S., Hotate, K., Herráez, M.G., and Thévenaz, L. (2006). Highly efficient Brillouin slow and fast light using As2Se3 chalcogenide fiber. Optic. Express *14*, 5860–5865.

Sun, Y.n., Dai, S., Zhang, P., Wang, X., Xu, Y., Liu, Z., Chen, F., Wu, Y., Zhang, Y., and Wang, R. (2015). Fabrication and characterization of multimaterial chalcogenide glass fiber tapers with high numerical apertures. Optic. Express *23*, 23472–23483.

Tai, K., Hasegawa, A., and Tomita, A. (1986). Observation of modulational instability in optical fibers. Phys. Rev. Lett. *56*, 135.

Tao, G., Ebendorff-Heidepriem, H., Stolyarov, A.M., Danto, S., Badding, J.V., Fink, Y., Ballato, J., and Abouraddy, A.F. (2015). Infrared fibers. Adv. Opt. Photon. *7*, 379–458.

Thurston, R. (1992). Elastic waves in rods and optical fibers. J. Sound Vib. *159*, 441–467.

Torres, B., Payá-Zaforteza, I., Calderón, P.A., and Adam, J.M. (2011). Analysis of the strain transfer in a new FBG sensor for structural health monitoring. Eng. Struct. *33*, 539–548.

Wang, J., Zhu, Y., Zhang, R., and Gauthier, D.J. (2011). FSBS resonances observed in a standard highly nonlinear fiber. Optic. Express *19*, 5339–5349.

Wang, Y., Dai, S., Han, X., Zhang, P., Liu, Y., Wang, X., and Sun, S. (2018). Broadband mid-infrared supercontinuum generation in novel As2Se3-As2Se2S step-index fibers. Opt. Commun. *410*, 410–415.

Webb, D.J. (2015). Fibre Bragg grating sensors in polymer optical fibres. Meas. Sci. Technol. *26*, 092004.

Xing, S., Grassani, D., Kharitonov, S., Billat, A., and Brès, C.-S. (2016). Characterization and modeling of microstructured chalcogenide fibers for efficient mid-infrared wavelength conversion. Optic. Express *24*, 9741–9750.

Xing, S., Grassani, D., Kharitonov, S., Brilland, L., Caillaud, C., Trolès, J., and Brès, C.-S. (2017). Mid-infrared continuous-wave parametric amplification in chalcogenide microstructured fibers. Optica *4*, 643–648.

Yu, F., Wadsworth, W.J., and Knight, J.C. (2012). Low loss silica hollow core fibers for 3–4 μm spectral region. Optic. Express *20*, 11153–11158.

Yuan, W., Khan, L., Webb, D.J., Kalli, K., Rasmussen, H.K., Stefani, A., and Bang, O. (2011). Humidity insensitive TOPAS polymer fiber Bragg grating sensor. Optic. Express *19*, 19731–19739.

Zhang, C., Zhang, W., Webb, D.J., and Peng, G.-D. (2010). Optical fibre temperature and humidity sensor. Electron. Lett. *46*, 643–644.